EYE-CLIMA
Verifying emissions of climate forcers

Final fluxes of CO_2, CH_4 and N_2O at 0.2° from 2018

DELIVERABLE D3.4

Author(s):	CEA: Grégoire Broquet, Antoine Berchet Science Partners: Audrey Fortems-Cheiney FMI: Anteneh Getachew Mengistu, Tuula Aalto, NILU: Nalini Krishnankutty
Date of submission:	17-02-2026
Version:	1.0
Responsible partner:	CEA
Deliverable due date:	30-04-2025
Dissemination level:	Public

Call:	HORIZON-CL5-2022-D1-02
Topic:	Climate Sciences and Responses
Project Type:	Research and Innovation Action
Lead Beneficiary:	NILU - Norsk Institutt for Luftforskning

This project has received funding from the European Union's Horizon Europe research and innovation programme under grant agreement No 101081395

Document History

Version	Date	Comment	Modifications made by
0.1	10-02-2026	First draft	Grégoire Broquet, Antoine Berchet, Audrey Fortems-Cheiney, Anteneh Getachew Mengistu, Tuula Aalto, and Nalini Krishnankutty
0.2	11-02-2026	Internal review	Rona Thompson
0.3	12-02-2026	Final version	Grégoire Broquet, Antoine Berchet, Audrey Fortems-Cheiney, Anteneh Getachew Mengistu, Tuula Aalto, and Nalini Krishnankutty
1.0	17-02-2026	Submitted to Commission	Rona Thompson

This project has received funding from the European Union's Horizon Europe research and innovation programme under grant agreement No 101081395

Summary

One of the main objectives of EYE-CLIMA is to support the verification of National Greenhouse Gas Inventories (NGHGIs) by providing estimates of greenhouse gas emissions based on atmospheric observations. Emissions estimates can be derived from observations through atmospheric inversions, and the use of this method to verify NGHGIs has been highlighted in the 2019 refinement of the IPCC Guidelines. However, the adoption of this type of verification has been hampered by the complexity of the method, the uncertainties and, hitherto, the limited resolution of the emission estimates.

EYE-CLIMA has a strong focus on improving both the accuracy and resolution of regional inversions. The accuracy of emissions derived from atmospheric inversions is expected to improve with higher spatial resolution due to improved resolution of the atmospheric transport, which should enable a better representation of the observations, as well as improved resolution of the fluxes (together reducing the model representation error). Moreover, higher spatial resolution will enable the borders of countries to be more accurately resolved. However, the higher spatial resolution presents several challenges.

In this context, the main objective of this deliverable is to perform inversions at higher spatial resolution, specifically 0.2°×0.2° and cover at least the period 2018 to 2023. The inversions at this resolution will not be extended further back in time than the start of the ICOS atmospheric record (or for CH_4, the launch of the TROPOMI instrument onboard the satellite Sentinel 5P) because prior to the start of these records, the observation coverage over Europe is poorer.

This deliverable presents the final results of the high-resolution (0.2°) regional inversions for CO_2, CH_4 and N_2O fluxes in Europe. CH_4 and N_2O inversions cover the period from 2018 to 2023, and CO_2 inversion results are shown for the period 2019-2022.

For CH_4, the results suggest prior inventories underestimated agricultural and combustion emissions in parts of northwestern and central Europe, and overestimated emissions in Italy, Romania, and the UK. Geological emissions were revised strongly downward, highlighting the need for region-specific parameterizations, while wetland emissions, especially in northern Europe in summer, were also reduced. Despite these adjustments, seasonal patterns remained realistic, with wetlands still driving summer CH_4 peaks. For the EU27+3 countries the six years mean total emissions increased slightly from 21.3 Tg yr^{-1} (prior) to 21.8 Tg yr^{-1} (posterior), corresponding to a change of +2.3%. Agricultureand waste CH_4 emissions increased by 17.1% and combustion by 1.5%, while geological (−59.7%) and wetland (−4.8%) emissions declined.

For N_2O, the inversion spans the period from 2018 to 2023. The posterior emissions are systematically higher than the prior, with the emission totals for EU27+3 increasing from 0.75 TgN_2O yr^{-1} (prior) to 1.01 TgN_2O yr^{-1} (posterior), consistent with an overall ~34.67% after optimisation. The largest positive adjustments occur in northwestern Europe, notably across the UK, northern France and Benelux region, indicating that the prior likely underestimated emissions in these source areas. In contrast, the inversion suggests reduced emissions over parts of northern Italy and central–eastern Europe, pointing to potential prior overestimation or redistribution of sources in these regions.

For CO_2, the inversions using surface measurements significantly improved the fit between the simulated and observed CO_2 mixing ratios. European ecosystems act as a CO_2 sink as the posterior estimate of the NEE+F_{LUC} average annual budget for EU27+3 over 2019-2022 is of about -0.78 $PgC.yr^{-1}$. This NEE+F_{LUC} estimate is 53% larger than the posterior estimate from surface measurements at the 0.5° spatial resolution of about -0.36 $PgC.yr^{-1}$ over the period 2019-2022 but relatively consistent with the satellite-based inversions at the 0.5° spatial resolution.

This project has received funding from the European Union's Horizon Europe research and innovation programme under grant agreement No 101081395

TABLE OF CONTENTS

This project has received funding from the European Union’s Horizon Europe research and innovation programme under grant agreement No 101081395

This project has received funding from the European Union's Horizon Europe research and innovation programme under grant agreement No 101081395

1. Introduction

One of the main objectives in EYE-CLIMA is to address the need for independent verification of National Greenhouse Gas Inventories (NGHGIs) by developing top-down methods based on atmospheric inversion (using both satellite remote sensing and ground-based observations) to a level of readiness where they can be used to determine emissions at national and sub-national scales. Towards this objective, this deliverable presents results of atmospheric inversions of CO_2, CH_4 and N_2O run at a spatial resolution of 0.2°×0.2° over Europe, focusing on EU27 countries plus UK, Switzerland and Norway (EU27+3).

Atmospheric inversions are a valuable method to constrain emission estimates using observations of atmospheric mixing ratios. The method involves using an atmospheric chemistry transport model (ACTM) to relate an existing independent estimate of the fluxes (the prior estimate) to atmospheric mixing ratios and to determine the model-observation error. This error is then used to update the prior estimate by effectively inverting the transport to relate the difference in mixing ratio to a difference in flux.

Although the atmospheric inversion methodology is well-established there is still room for substantial improvements. The spatial resolution of regional inversions prior to EYE-CLIMA was typically around 0.5° (e.g. EUROCOM, VERIFY and RECCAP-2), but improving the resolution should improve the representation of observations by the atmospheric transport model, and it will improve the resolution of the fluxes, together this should result in a reduction of the model representation error.

The overall aim of this deliverable is to perform European inversions for CO_2, CH_4 and N_2O for at least the period 2018 to 2023, i.e., when there are sufficiently dense observations (when observations are available from ICOS, OCO-2 for CO_2 and from TROPOMI for CH_4).

The inversions are performed using the Community Inversion Framework (CIF) combined with the FLEXPART or CHIMERE models.

2. Methodology

2.1. Inversion framework

The Community Inversion Framework (CIF) is an open-source inversion framework and was developed with the intention of concentrating inversion developments into a community code and to be interfaced with different atmospheric transport models (Berchet et al., 2021). In EYE-CLIMA, the CIF is interfaced with two atmospheric transport models, FLEXPART and CHIMERE (see Section 2.2).

For the high-resolution inversions, we use the Community Inversion Framework's (CIF) four-dimensional variational (4DVAR) optimization approach (Berchet et al., 2021). The inversion algorithm minimizes the following cost function $J(\mathbf{x})$ with respect to the state vector $\mathbf{x}$:

$$J(\boldsymbol{x}) = \frac{1}{2}(\boldsymbol{x}-\boldsymbol{x_b})^{\mathrm{T}}\mathbf{B}^{-1}(\boldsymbol{x}-\boldsymbol{x_b}) + \frac{1}{2}(H(\boldsymbol{x})-\boldsymbol{y})^{\mathrm{T}}\mathbf{R}^{-1}(H(\boldsymbol{x})-\boldsymbol{y}) \quad (1)$$

Here, $\mathbf{x}$ represents the state vector of model variables, $\mathbf{x_b}$ is the initial guess or prior state vector, $\mathbf{B}$ denotes the background error covariance matrix reflecting uncertainties in $\mathbf{x_b}$, $\mathbf{y}$ is the vector of observed data, $H(\mathbf{x})$ is the observation operator mapping $\mathbf{x}$ to the observation space, and $\mathbf{R}$ is the observation error covariance matrix accounting for uncertainties in $\mathbf{y}$. The first term on the right-hand side of Eq. 1

This project has received funding from the European Union's Horizon Europe research and innovation programme under grant agreement No 101081395

represents the distance from the prior state $\mathbf{x_b}$ and second term represents the distance from observations.

To minimize $J(\mathbf{x})$, the gradient $\nabla J(\mathbf{x})$ is computed:

$$\nabla J(\boldsymbol{x}) = \mathbf{B}^{-1}(\boldsymbol{x} - \boldsymbol{x_b}) + \left(H'(\boldsymbol{x})\right)^{\mathrm{T}}\mathbf{R}^{-1}(H(\boldsymbol{x}) - \boldsymbol{y}) \quad (2)$$

The conjugate gradient algorithm (Lanczos, 1950) utilizes $\nabla J(\mathbf{x})$ to iteratively update $\mathbf{x}$, continuing until the gradient norm falls below a predefined threshold or a maximum number of iterations is reached.

2.2. Atmospheric transport models

In this deliverable, two different atmospheric transport models are used, the Lagrangian Particle Dispersion Model (LPMD), FLEXPART, and the regional Eulerian model, CHIMERE. These models are described below.

2.2.1. FLEXPART

FLEXPART models the dispersion and turbulent mixing of gases and aerosols in the atmosphere using virtual particles (Stohl et al. in 1995; Pisso et al. in 2019). In this deliverable, two versions of FLEXPART are used, i.e., v10.4 and v11 (released 2024). One of the main differences in v11 is the possibility to perform the transport calculations on the original grid of the meteorological input fields, which brings some improvements to the accuracy. In this study, the meteorological reanalysis data from the European Centre for Medium-Range Weather Forecasts (ECMWF) ERA5 (Hittmeir et al. 2018) is used to drive FLEXPART. The ERA5 data are available at hourly intervals and span 137 vertical layers.

FLEXPART is run to generate source-receptor relationships (SRRs), which describe the relationship between change in observed mixing ratio and the fluxes. The SRRs are used in the inversion framework (CIF) to model atmospheric mixing ratios as well as to relate the model-observation differences to a correction to the prior fluxes.

For each observation, a 10-day backward transport simulation is made using the FLEXPART to produce the SRRs. These SRRs are saved with a resolution of 0.2°×0.2° for the nested domain over Europe, and at 2°×2° for the global domain, all of which are stored at hourly intervals. For atmospheric greenhouse gases like CH_4 and N_2O which have long atmospheric lifetime, a background mixing ratio estimate is needed, which accounts for the influence on the observation prior to the start of the backward trajectory calculation. This is determined by coupling the end points of the particle trajectories to 3D initial mixing ratio fields of the target species, which may be obtained from a global model (Thompson and Stohl, 2014).

2.2.2. CHIMERE

CHIMERE is an Eulerian chemistry-transport model (Menut et al., 2013; Mailler et al., 2017). The specific configuration, used here for the simulations of CO_2 concentrations and for the quantification of the terrestrial ecosystem at the relatively high spatial resolution of 0.2° over Europe, is detailed in Section 5.

This project has received funding from the European Union's Horizon Europe research and innovation programme under grant agreement No 101081395

3. CH_4 inversions

This section describes the CIF-FLEXPART CH_4 inversion configuration for Europe, spanning 11°W to 34°E and 34°N to 72°N, at a spatial resolution of 0.2° × 0.2°, covering the period 2018–2023. The inversion employs a 4D-Var framework to optimization CH_4 fluxes estimates from different sectors at the pixel level. Source–receptor relationships are quantified using the FLEXPART Lagrangian particle dispersion model, which provides the sensitivity matrix required for the inversion, as detailed in Section 2.

3.1. Prior fluxes

The prior CH_4 emission estimates were categorized into sectors: Fugitives from fossil fuels (FFF), Combustion (COM), Agriculture and waste (AGW), Wetlands, freshwater, and soil sinks (WET), Biomass burning (BBR), Geological (GEO), Termites (TER), and Ocean (OCE). Figure 3.1 displays the spatial distribution of these fluxes over the inversion domain. All sectors were independently optimized using predefined prior uncertainties as summarized in Table 1, except for termite and ocean fluxes, which were kept fixed during the inversion.

For anthropogenic emissions, monthly prior fluxes were obtained from the GAINS v2 inventory for EU27+3 countries (Deliverable D2.8) and from EDGAR2024 for the rest of the world (hereafter GAINS–EDGAR). Both GAINS and EDGAR provide data at a spatial resolution of 0.1° × 0.1° and monthly temporal resolution. Within GAINS v2, the subcategories include:

- *Fugitives (FFF): fugitive emissions from fossil fuels (D_Fugitives),*
- *Combustion (COM): emissions from public power (A_PublicPower), industry (B_Industry), other stationary combustion (C_OtherStationaryComb), and road transport (F_RoadTransport),*
- *Agriculture and waste (AGW): emissions from waste (J_Waste), livestock (K_AgriLivestock), and other agricultural activities (L_AgriOther).*

Biomass burning (BBR) emissions were taken from GFAS, covering emissions from open biomass burning. For wetland and soil fluxes, prior estimates within the European domain were derived from the JSBACH–HIMMELI ecosystem model (Deliverable D2.3). This model framework combines JSBACH land-ecosystem model with HIMMELI wetland model to simulate peatland, inundated soil, and mineral soil emissions, and provides wetland and soil CH_4 fluxes at a spatial resolution of 0.125° × 0.125° and daily temporal resolution. Additionally, freshwater fluxes were included following Johnson et al. (2022) for lakes and Rocher-Ros et al. (2023) for rivers, with global lake totals scaled to 13 Tg yr^{-1}, consistent with the lower-limit estimate of the Global Methane Budget (Saunois et al., 2024). The freshwater fluxes were originally at a spatial resolution of 0.25° × 0.25° and temporal resolutions of daily (lakes) and monthly (rivers). Geological fluxes (GEO) were taken from Etiope et al. (2019), representing onshore geological sources, and scaled globally to 15 Tg yr^{-1} following Saunois et al. (2024). Ocean emissions (OCE) were based on the climatological dataset of Weber et al. (2019), which accounts for both diffusive and ebullitive fluxes. Finally, termite emissions (TER) were prescribed from Castaldi (2013) and Saunois et al. (2024). As with the ocean fluxes, termite emissions were not optimized in the inversion but retained as fixed prior contributions. Geological, ocean and termite emissions were originally at a spatial resolution of 1° × 1° and monthly temporal resolution. All data are re-gridded to 0.2° × 0.2° × monthly resolution for the inversions.

This project has received funding from the European Union's Horizon Europe research and innovation programme under grant agreement No 101081395

Table 1. Prior CH_4 flux categories, source sectors, and inversion settings (optimization resolution, uncertainties, and correlations). TER and OCE are prescribed but not optimized.

Category abbreviations	Source Sectors	Optimization resolutions		Uncertainties	Correlations	
		Spatial	Temporal		Spatial	Temporal
FFF	Fugitives from fossil fuels	0.2° × 0.2°	Monthly	15%	100 km	1M
COM	Combustion	0.2° × 0.2°	Monthly	51%	100 km	3M
AGW	Agriculture and waste	0.2° × 0.2°	Monthly	80%	100 km	3M
WET	Wetlands, soil sinks and freshwater	0.2° × 0.2°	Monthly	100%	100 km	1M
BBR	Biomass burning	0.2° × 0.2°	Monthly	50%	50 km	1M
GEO	Geological	0.2° × 0.2°	Monthly	100%	300 km	6M
TER	Termites	N/A	N/A	N/A	N/A	N/A
OCE	Ocean	N/A	N/A	N/A	N/A	N/A

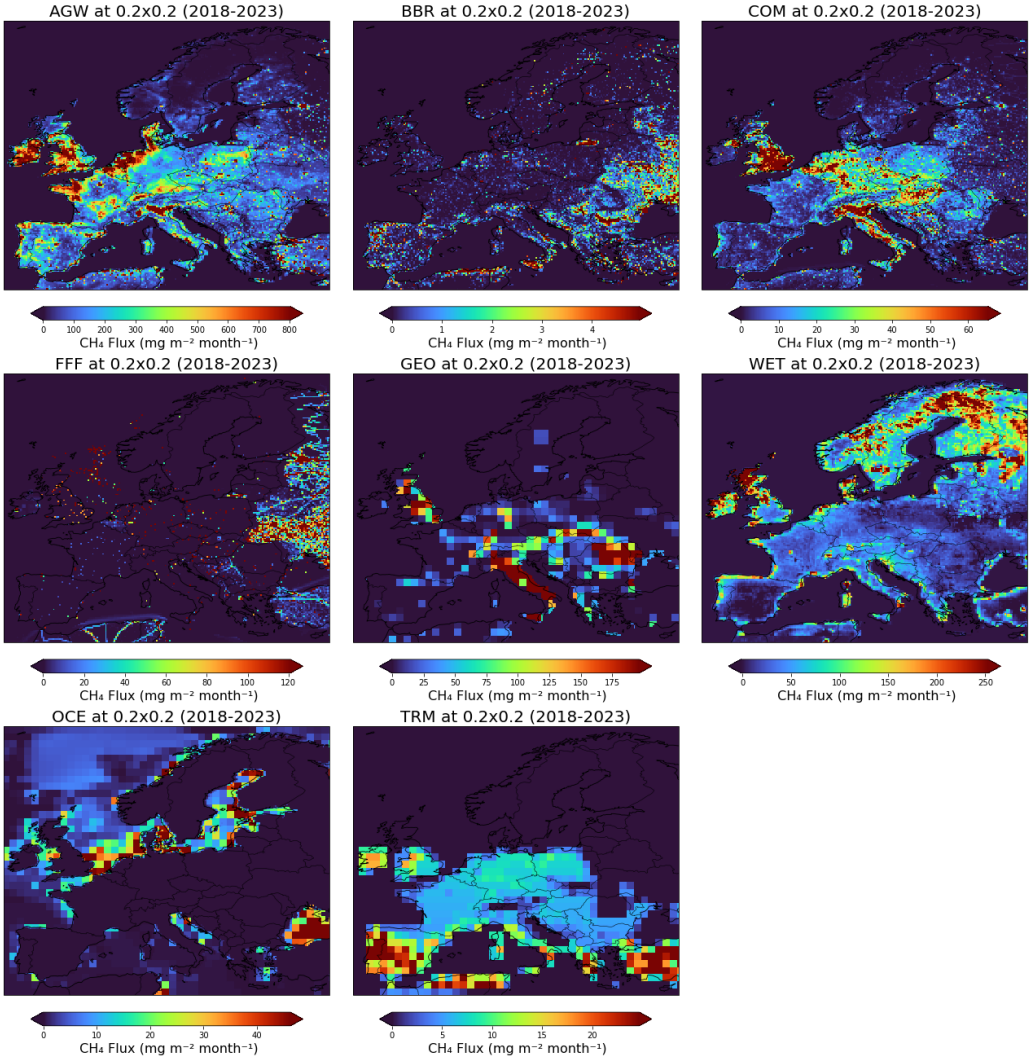

Figure 3.1: Annual mean prior methane emissions by source sampled for 2021. Note that the colour-scales of the maps vary.

This project has received funding from the European Union's Horizon Europe research and innovation programme under grant agreement No 101081395

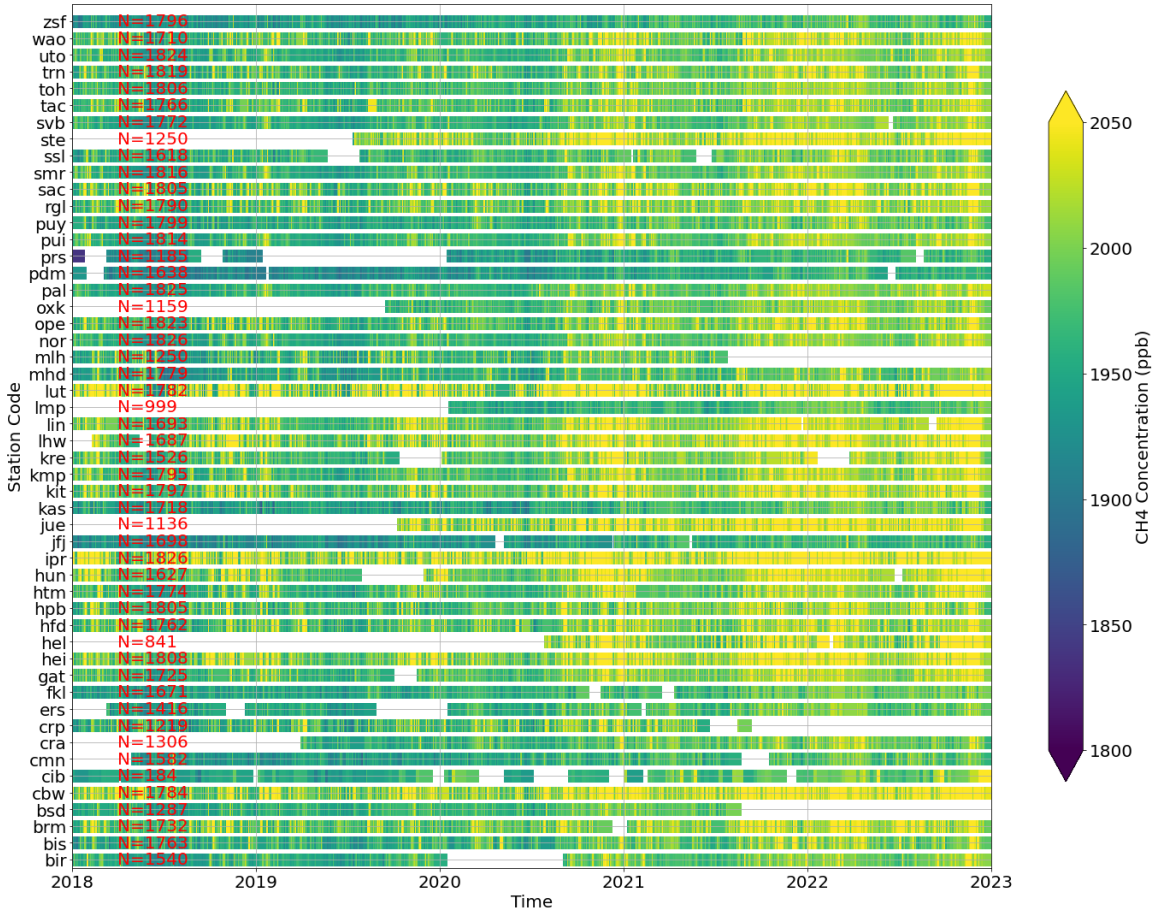

Figure 3.2: Overview of daily mean observational methane concentration from 2018 to 2023. White gaps indicate periods with no data available. The colour bar shows observed CH_4 concentrations in ppb, with each station represented by its 3-letter code on the y-axis. The red text indicates the total number of observations for each station over the full study period.

3.2. Observations

The Integrated Carbon Observation System (ICOS) offers a European compilation of atmospheric CH_4 mole fraction time series data. For the inversions, we used the data from ICOS ObsPack v10 (ICOS RI et al, 2024) and ICOS ATC OBSPACK-Europe-L2-2022 (Apadula et al., 2022). The sites which have more than 50% of data coverage during the study period are selected. In addition, the sites too close to each other are limited as those would not provide additional information about the fluxes. The sites that did not meet those criteria will be later used for validation. These datasets include both quality-controlled ICOS-labelled and non-labelled datasets. For data density and ICOS labelling see Figure 3.2. In addition to the ICOS data, pre-ICOS continuous hourly observations at Ochsenkopf, Germany (OXK) are taken from the VERIFY project (Thompson et al., 2021). The discrete observations at Centro de Investigacion de la Baja Atmosfera, Spain (CIB) are taken from the NOAA ObsPack GLOBALVIEWplusv7.0 (Schuldt et al., 2024) and continuous hourly observations from Kumpula, Finland (KMP) from the Finnish Meteorological Institute (FMI). The CIB data has approximately weekly resolution. The KMP data taken using similar measurement and calibration methods as other FMI stations, which are part of ICOS. Their geographical distribution across Europe is depicted in Figure 3.3. In cases where multiple intake heights were available, such as at the Cabauw station with intake heights at 27, 67, 127, and 207 meters above ground level, we opted to assimilate data solely from the highest intake height. This approach was taken to ensure that the assimilated data represent well-mixed conditions and not just very local influences. We assimilate hourly observations between 14:00 - 16:00 local time for low altitude stations (<= 1000 m.a.s.l) and between 02:00 - 04:00 local time for high-altitude stations (> 1000 m.a.s.l).

This project has received funding from the European Union's Horizon Europe research and innovation programme under grant agreement No 101081395

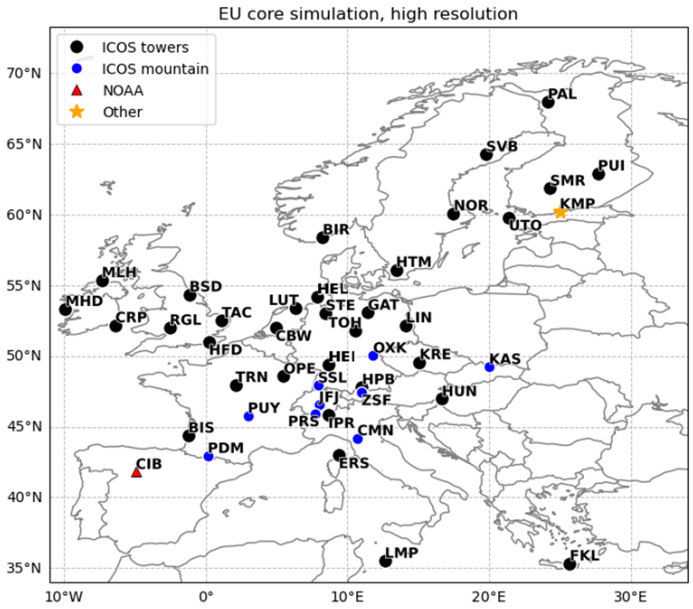

Figure 3.3: Geographic distribution of sites used in data assimilation. Blue dotes refer to mountain stations above (1000 masl) while black dotes are low altitude stations.

3.3 Results

3.3.1 Comparison of Modelled and observed CH_4 mixing ratio

Figure 3.4 presents representative time series of CH_4 concentrations from six assimilated observation sites: Cabauw (CBW, Netherlands), Ispra (IPR, Italy), Pallas (PAL, Finland), Steinkimmen (STE, Germany), Plateau Rosa (PRS, Italy), and Centro de Investigación de la Baja Atmósfera (CIB, Spain). The observed time series from ObsPack are compared with prior and posterior simulations from the CIF-FLEXPART inversion, performed at a spatial resolution of 0.2° × 0.2° for the period 2018–2023. Across all stations, the posterior estimates show a clear improvement in reproducing observed variability relative to the prior. Posterior simulations more closely track the measured time series, capturing both baseline concentrations and short-term enhancements linked to regional-scale emissions. The inset scatterplots quantify these improvements, with posterior estimates consistently showing reduced root mean square error (RMSE) and bias compared to the prior. At Cabauw, for example, RMSE decreased from 67.01 ppb in the prior to 38.86 ppb in the posterior, while bias improved from –43.65 ppb to –13.22 ppb. Similar patterns are observed at Ispra and CIB, where prior simulations systematically underestimated concentrations, and posterior corrections significantly reduced these mismatches. At background and high-altitude sites such as Pallas and Plateau Rosa, the adjustments are smaller, reflecting their role in constraining large-scale background concentrations rather than local emission plumes.

This project has received funding from the European Union's Horizon Europe research and innovation programme under grant agreement No 101081395

Figure 3.5 provides a network-wide statistical evaluation of model performance across all assimilated sites. Three metrics are shown: (a) bias, (b) RMSE, and (c) correlation coefficient. Posterior bias is consistently reduced across nearly all stations, with particularly large corrections at Ispra, where the strong negative prior bias (> –60 ppb) is substantially corrected. RMSE values decrease systematically across the network, with reductions often exceeding 30%, especially at continental stations influenced by regional emissions (e.g., Cabauw, Ispra, Steinkimmen). Correlation coefficients between modelled and observed CH_4 concentrations also improve notably in the posterior, frequently exceeding 0.8. This highlights the improved skill of the inversion system in reproducing temporal variability.

Overall, the results demonstrate that the CIF-FLEXPART inversion at 0.2° × 0.2° resolution effectively assimilates observational constraints, reducing systematic errors and improving the temporal and spatial representation of CH_4 across Europe. The improvements in bias, RMSE, and correlation collectively underscore the robustness of the inversion framework in refining regional methane emission estimates.

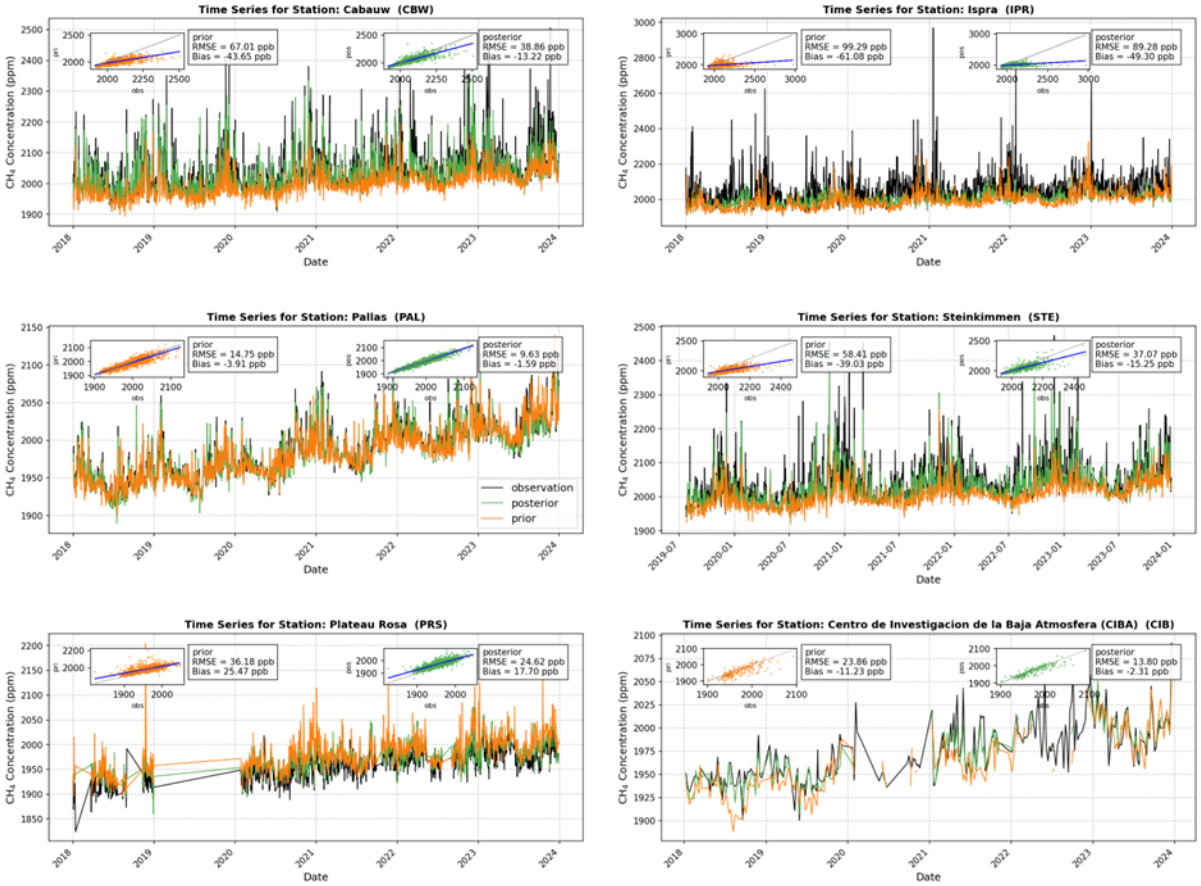

Figure 3.4: Time series of CH_4 concentrations sampled at six assimilated stations. Observations from ObsPack (black) are compared with CIF-FLEXPART inversion results for posterior concentrations (green) and prior concentrations (orange).

This project has received funding from the European Union's Horizon Europe research and innovation programme under grant agreement No 101081395

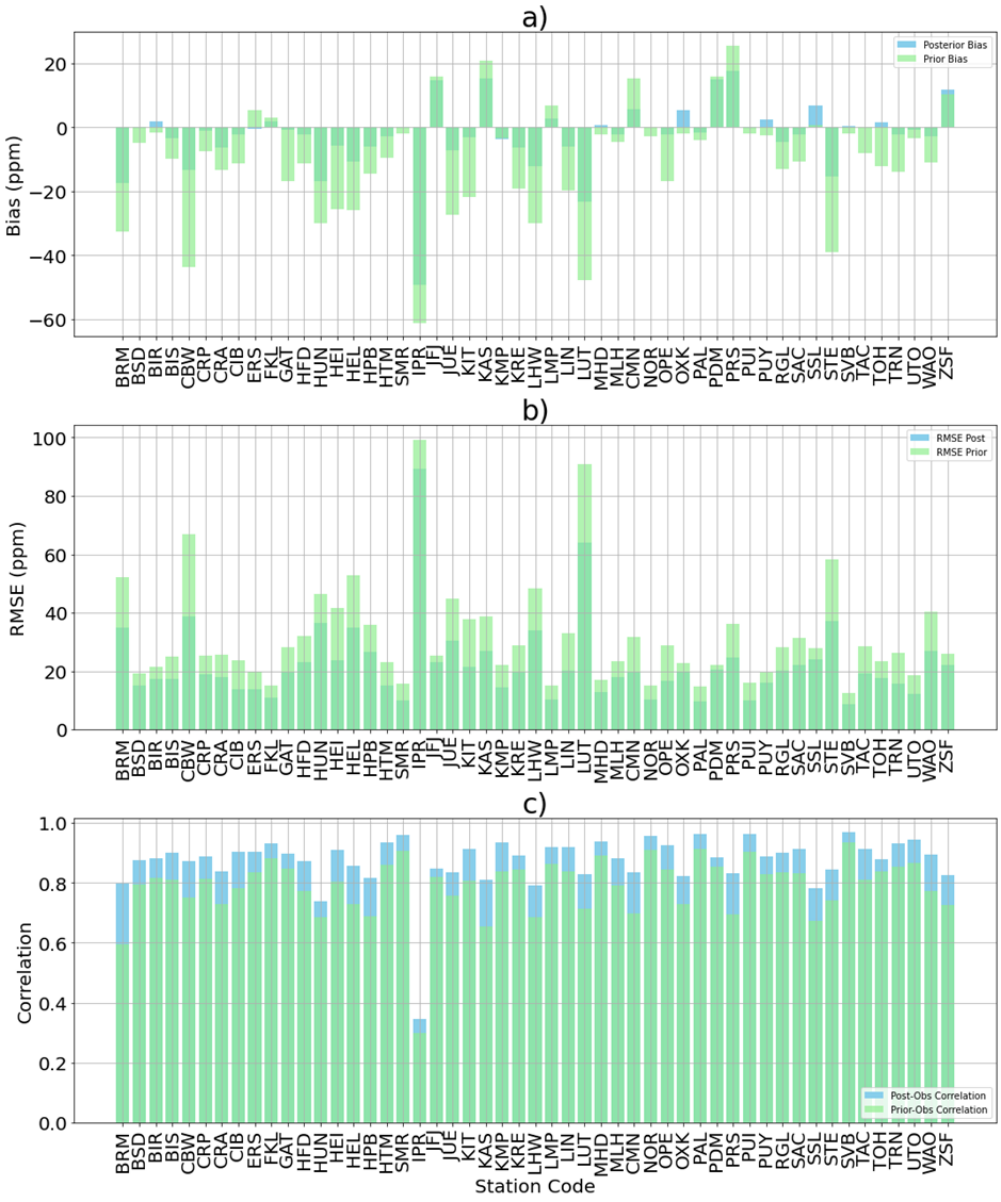

Figure 3.5: Overview of statistical results for assimilated observed concentration and CIF-FLEXPART posterior and prior simulated concentrations from all stations used in the inversion.

3.3.2 Spatial distribution of prior and posterior fluxes

Figure 3.6 presents the spatial distribution of mean methane (CH_4) emissions across Europe over the period 2018–2023, derived from our CIF-FLEXPART inversion system at a high spatial resolution of 0.2° × 0.2°. The figure is divided into three panels: the left panel shows the prior emission estimates, the middle panel displays the posterior estimates, and the right panel illustrates the posterior increment, defined as the difference between posterior and prior emissions.

The posterior estimates reveal notable regional adjustments compared to the prior. Specifically, CH_4 emissions from agricultural and combustion sectors exhibit significant increases over the Netherlands, Germany, and France, suggesting that prior inventories may have underestimated emissions in these regions. Conversely, Italy and Romania, show a reduction in posterior emissions, particularly in the

This project has received funding from the European Union's Horizon Europe research and innovation programme under grant agreement No 101081395

geological sector, indicating potential overestimation in the prior data and a reduction over northern United Kingdom in the wetland sector.

Emissions from fossil fuel sources generally show a reduction across most European regions, with localized increases observed in Belgium, Luxembourg, Eastern Ukraine, and parts of Russia. These regional enhancements may reflect underreported activities or inventory gaps in the prior data.

Geological emissions show a substantial reduction in Italy and Romania, likely due to inflated prior estimates influenced by globally scaled geological emission factors. Although the global geological CH_4 emissions were scaled to 15 Tg yr^{-1}, the results suggest that further refinement is needed, either through region-specific scaling or hotspot-targeted adjustments rather than applying a uniform scaling factor. This finding aligns with discrepancies noted in Figure 3.1 and highlights the importance of spatially adaptive scaling in inversion frameworks.

Wetland emissions show a general reduction over Scandinavian countries, primarily driven by decreased summer fluxes (June–August), which are not explicitly shown in the figure. This seasonal reduction is likely due to prior overestimation of summer CH_4 emissions in northern latitudes.

Aggregated over the EU27+3 countries, the inversion results indicate an overall increase in total emissions from 21.3 Tg yr^{-1} (prior) to 21.8 Tg yr^{-1} (posterior), corresponding to a change of +2.3%. By sector, agricultural emissions (AGW) increased from 13.0 to 15.2 Tg yr^{-1} (+17.1%), biomass burning (BBR) remained essentially unchanged at 0.04 Tg yr^{-1} (0.0%), combustion emissions (COM) slightly increased from 0.9 to 1 Tg yr^{-1} (+1.5%), fossil fuel emissions (FFF) slightly decreased from 1.08 to 1.07 Tg yr^{-1} (−1%), geological emissions (GEO) dropped markedly from 2.6 to 1.0 Tg yr^{-1} (−59.7%), and wetland emissions (WET) declined from 3.7 to 3.5 Tg yr^{-1} (−4.8%) (See table 3.4).

*Table 3.1 Annual prior and posterior CH_4 emissions for the EU27+3 countries and their relative posterior increment, defined as Δ% (posterior * 100/prior) −100, expressed in percent.*

year	Total			AGW			COM			FOS			GEO			WET		
	Prior	Post	Δ%	Prior	Post	Δ%	Prior	Post	Δ%	Prior	Post	Δ%	Prior	Post	Δ%	Prior	Post	Δ%
2018	22.2	23.2	4.5	13.7	16.3	19.1	1.0	1.0	1.7	1.3	1.2	-3.2	2.6	1.3	-50.1	3.6	3.4	-8.0
2019	21.8	21.8	0.2	13.5	15.3	13.4	1.0	1.0	1.4	1.2	1.2	-0.8	2.6	1.0	-62.2	3.6	3.4	-4.6
2020	21.9	21.1	-3.5	13.3	14.5	9.2	0.9	1.0	1.0	1.0	1.0	-0.7	2.6	0.8	-69.2	3.9	3.7	-5.2
2021	21.3	21.3	0.2	12.9	14.7	13.7	1.0	1.0	1.6	1.0	1.0	-1.2	2.6	1.0	-59.8	3.7	3.5	-5.0
2022	20.1	21.9	8.8	12.2	15.5	27.2	0.9	0.9	2.0	1.0	1.0	-0.8	2.6	1.1	-57.2	3.4	3.3	-1.8
2023	20.7	21.5	3.7	12.4	14.9	20.0	0.8	0.9	1.6	1.0	1.0	-0.6	2.6	1.0	-60.0	3.8	3.6	-4.4

This project has received funding from the European Union's Horizon Europe research and innovation programme under grant agreement No 101081395

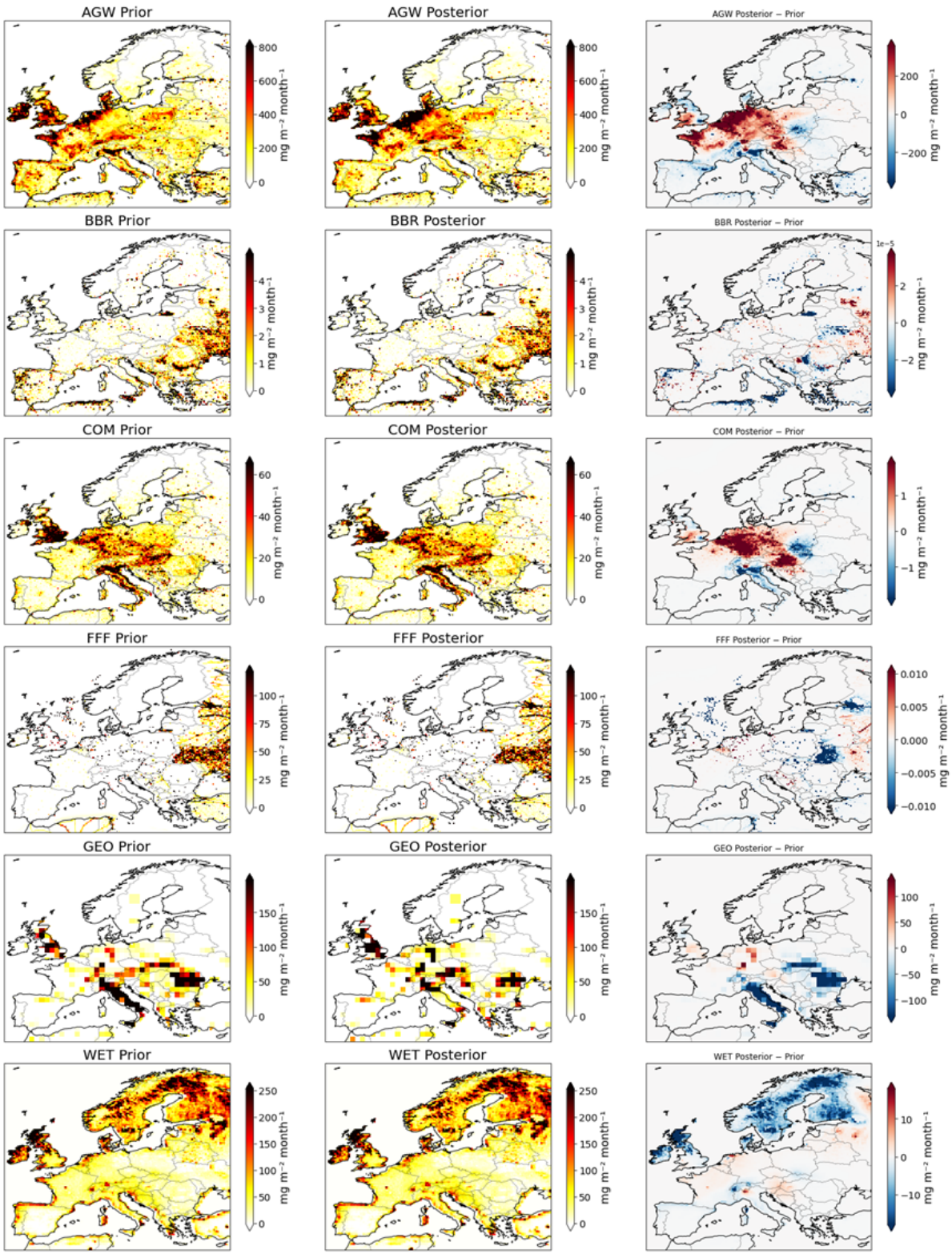

Figure 3.6: Mean spatial distribution of CH_4 fluxes from the CIF-FLEXPART inversion (2018–2023) at 0.2° × 0.2° resolution for the optimized emissions form the six sectors. Shown are prior (left), posterior (middle), and posterior–prior increments (right).

Figure 3.7 presents the time series of total and sectoral methane (CH_4) emissions spatially averaged for EU27+3 countries for the years 2018 and 2023. The total CH_4 emissions exhibit a pronounced seasonal cycle, primarily driven by wetland emissions, which peak during the summer months. In contrast, emissions from combustion sources have a seasonal cycle that is 6 months out of phase with that of

This project has received funding from the European Union's Horizon Europe research and innovation programme under grant agreement No 101081395

wetlands with maxima occurring in winter. Emissions from other sectors do not show a consistent seasonal pattern.

Posterior estimates reveal that emissions from the agricultural sector consistently exceed prior inventory values across most years. Conversely, geological emissions are generally lower in the posterior estimates. Wetland emissions also show reduced values during summer, contributing to a lower total posterior flux compared to prior estimates, particularly in the summer months. This seasonal reduction appears to intensify over time.

In 2018, posterior total emissions were markedly above average (23.2 Tg yr^{-1}; z-score = 5.63), driven largely by greater AGW emissions (16.3 Tg yr^{-1}; z-score = 3.87) and GEO (1.3 Tg yr^{-1}; z-score = 2.85). Wetland emissions from May to August were adjusted downward from 4.4 Tg yr^{-1} in the prior to 3.9 Tg yr^{-1} in the posterior, representing a statistically significant negative correction (z-score = −2.61) relative to other years. These findings are consistent with the 0.5° inversion, which produced a slightly higher posterior total (23.5 Tg yr^{-1}), along with a weaker AGW contribution (15.5 Tg yr^{-1}) and a notably stronger GEO contribution (2.7 Tg yr^{-1}). This highlights differences in the inferred source partitioning between the two inversion setups. In 2020, posterior total emissions (21.1 Tg yr^{-1}; z-score = −1.3) were below the interannual mean, though not significantly so. AGW remained within normal variability (14.5 Tg yr^{-1}; z-score = −1.4), GEO declined significantly (0.8 Tg yr^{-1}; z-score = −2.7), and WET was anomalously high (3.7 Tg yr^{-1}; z-score = 2.58), driven in part by elevated winter emissions. The 0.5° inversion produced a slightly lower total (20.2 Tg yr^{-1}), with marginally reduced AGW (14.1 Tg yr^{-1}) and WET (3.3 Tg yr^{-1}) estimates, while GEO remained essentially unchanged (0.8 Tg yr^{-1}).

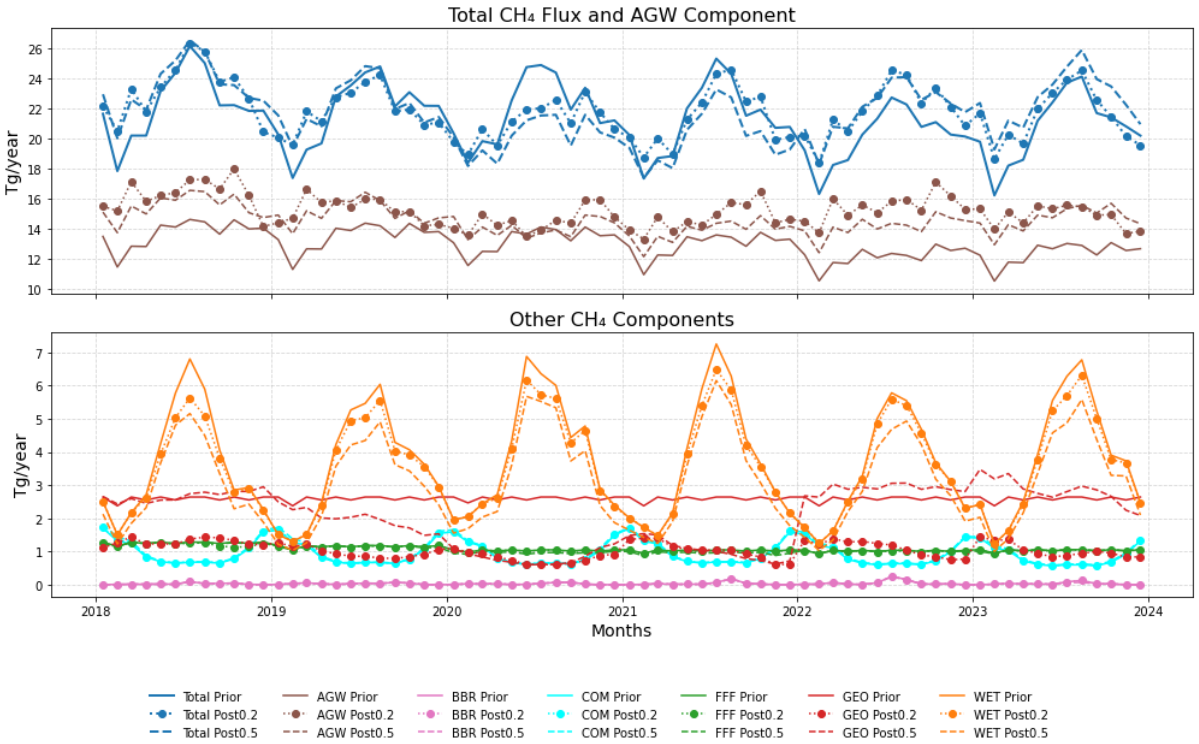

Figure 3.7: Time series of monthly mean total and sectoral CH_4 emissions spatially aggregated for the EU27+3 countries for the period 2018–2023. The results for the 0.5° inversions are also shown (dashed lines).

This project has received funding from the European Union's Horizon Europe research and innovation programme under grant agreement No 101081395

4. N_2O inversions

This section outlines the configuration used in the CIF-FLEXPART system for inversions of nitrous oxide (N_2O) over Europe. The nested domain for N_2O inversions spans from 11°W to 35°E in longitude and 34°N to 72°N in latitude, as illustrated in Figure 4.1 below.

4.1 Model set-up

For the N_2O inversions, the FLEXPART version 11 (FLEXPART-v11) was modified to simultaneously output data for two nested domains at spatial resolutions of 0.5° and 0.2°. This enhancement enables a single model run to provide results at both resolutions, significantly improving computational efficiency.

A variable-resolution grid was defined for the inversion as shown in Figure 4.1. The grid is defined based on the SRRs and the prior fluxes following the method of Thompson and Stohl (2014). The grid cells in the domain correspond to aggregates of 1.6°, 0.8°, 0.4°, and 0.2° resolution. Here, grid cells are aggregated where there is little information provided by the observations about the fluxes. Using an aggregated grid has the advantage of reducing the dimension of the inversion problem, thus reducing the computation time and memory required, while avoiding introducing aggregation error.

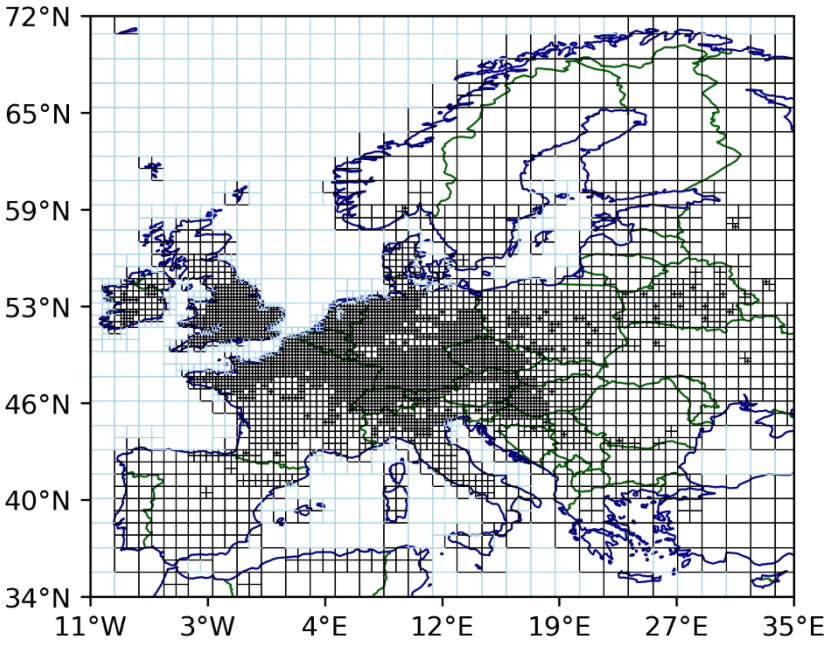

Figure 4.1: Variable-resolution grid used in the inversion

4.2. Prior Fluxes

To perform the inversion, we incorporated monthly prior flux estimates from various key sources: agricultural emissions, other anthropogenic emissions, biomass burning emissions, emissions from "natural" soils, as well as climatological estimates for ocean emissions. Figure 4.2 illustrates the spatial distribution of these fluxes over the inversion domain.

The monthly emission data for agriculture and other anthropogenic sources were obtained from the GAINS model (Greenhouse gas – Air pollution Interactions and Synergies), specifically the dataset provided in Deliverable D2.8. This data covers the EU27+3 countries.

This project has received funding from the European Union's Horizon Europe research and innovation programme under grant agreement No 101081395

- *Agricultural emissions* include both direct and indirect sources and encompass manure management.
- *Other anthropogenic emissions* refer to emissions from transportation, industrial activities, and waste management.

Prior flux estimates for biomass burning were derived from the GFEDv4.1 dataset (Randerson et al., 2017). To avoid double-counting, agricultural waste burning was excluded from this dataset, as it is already accounted for in the GAINS agricultural sector. Emissions from unmanaged (natural) soils were provided by the O-CN land surface model. These represent the natural background N_2O fluxes in the absence of human activity. Prior oceanic fluxes were based on climatological simulations from the PlankTOM ocean biogeochemistry model. These represent a seasonal baseline of N_2O fluxes between the ocean and atmosphere.

The prior flux data provides the starting point for the inversion, but the model optimizes the total N_2O flux by combining all sources and adjusting their contributions based on atmospheric observations and transport modelling.

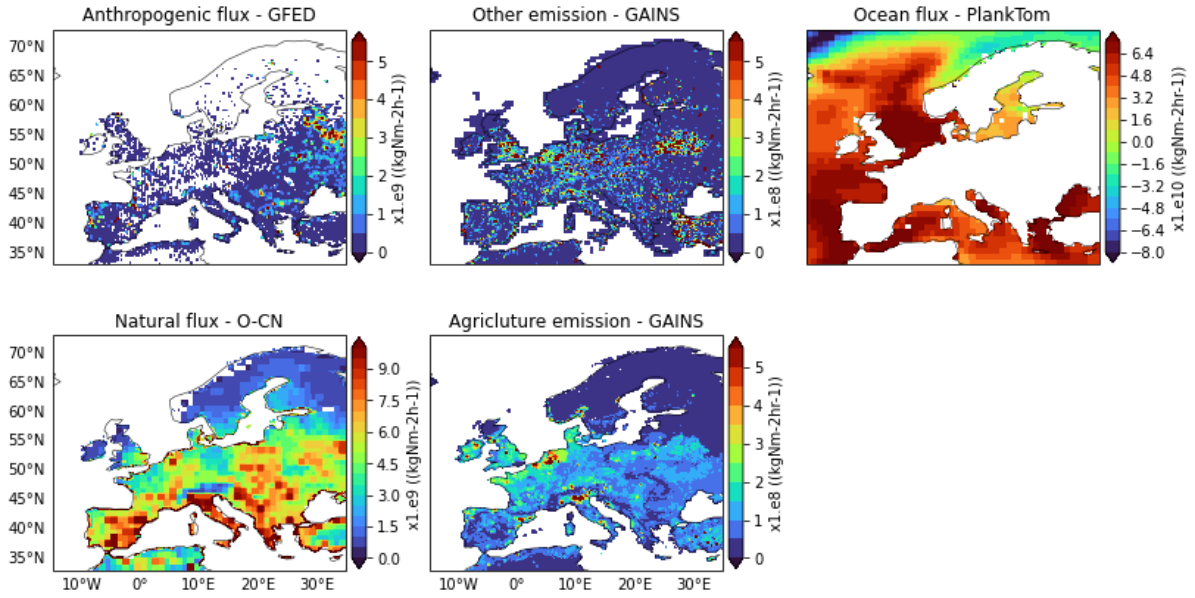

Figure 4.2: Annual mean N_2O emissions at 0.1°x0.1° resolution for 2019. Note that the scales of the maps vary

4.3 Observations

The N_2O observations for Europe were compiled through a collaborative effort between the EYE-CLIMA, AVENGERS, and PARIS projects. This observational dataset forms a critical component of the inversion framework by providing constraints on the spatiotemporal distribution of N_2O emissions. The dataset includes measurements from 30 stations across Europe, with valid observations beginning in 2018. The data sources include InGOS project (pre-ICOS), the ICOS atmospheric network, the World Data Centre for Greenhouse Gases (WDCGG), and the NOAA discrete (flask) sampling network (Henne et al., 2024). These data have been compiled and quality-controlled following protocols described in Henne et al. (2024) and are publicly accessible through the https://meta.icos-cp.eu/collections/FHIS-w3c_eny9-NDoR7ddvTX. The geographical distribution of sites across Europe is depicted in Figure 4.3, with markers colour-coded by altitude. Observational altitudes range from sea level up to approximately 2500 meters above sea level (masl). For sites with multiple sampling heights, only measurements from the

This project has received funding from the European Union's Horizon Europe research and innovation programme under grant agreement No 101081395

highest intake level were used. This approach ensures better representation of the free troposphere and reduces surface-layer influences.

The temporal availability of N_2O observations across the 30 monitoring sites is illustrated in Figure 4.4. This figure presents a heatmap of the number of months with valid data for each site over the inversion period from 2018 to 2023. Colour coding reflects the number of months with data available per year, ranging from 0 (no data) to 12 months (full year coverage). Most stations exhibit continuous observations throughout the inversion period, particularly from 2020 onward. Some stations display gaps in early years (2018–2019) due to site establishment dates or incomplete data transfer from earlier networks such as InGOS and pre-ICOS phases.

However, the orography in the meteorological data used in the transport model is only resolved at 0.5° and thus the altitude of the mountain sites in the model will be lower than in reality. Hence, the particle release heights in FLEXPART have been adjusted for the mountain sites (defined as > 1000 masl), to be the mid-point between the actual altitude of the sites and the altitude given by the meteorology, improving representativeness of atmospheric transport simulations. This treatment ensures a more physically realistic linkage between surface fluxes and atmospheric observations, particularly in topographically complex regions.

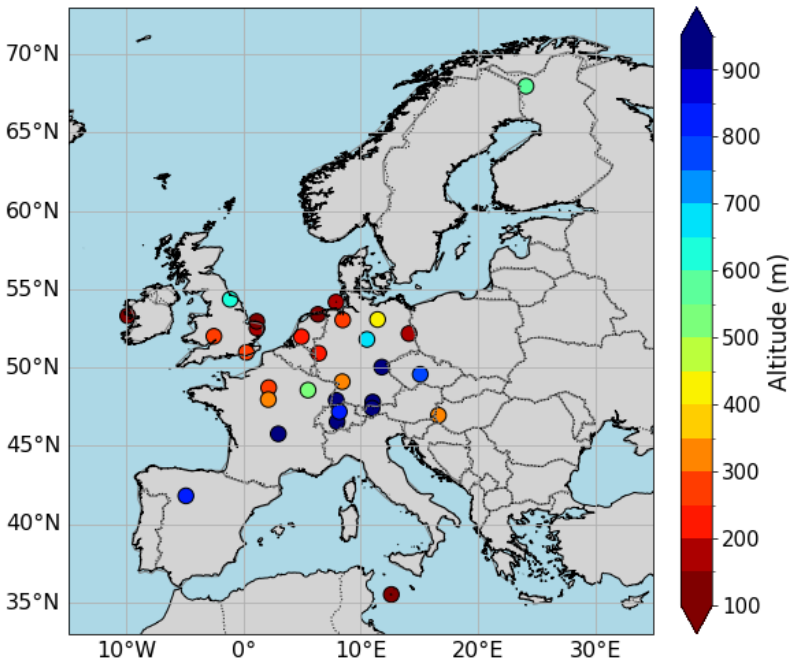

Figure 4.3: Geographical distribution of the sites showing also their altitude

This project has received funding from the European Union's Horizon Europe research and innovation programme under grant agreement No 101081395

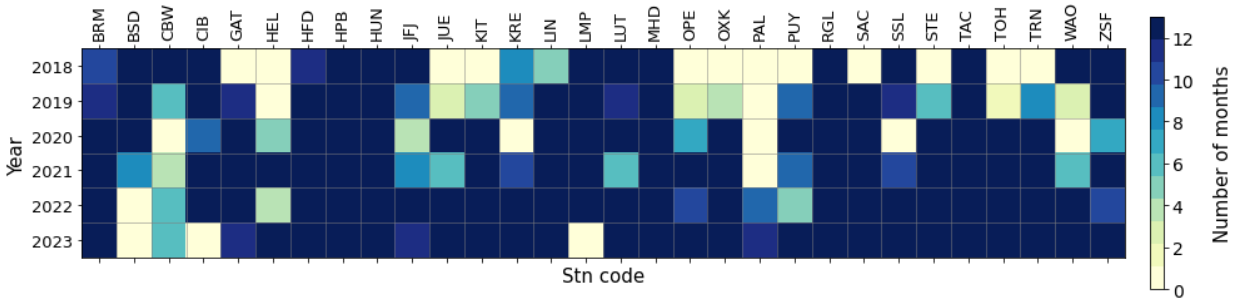

Figure 4.4: Data density in months for each site per year

4.4 Results

4.4.1 Modelled and observed atmospheric N_2O mole fractions

Figure 4.5 shows daily time series of observed N_2O mole fractions (black dots) and modelled values based on prior (green) and posterior (red) simulations for selected stations: BSD, HFD, KIT, LIN, and RGL. The time series spans from 2018 to 2023 (or up to each station's availability) and highlight the model's capability to reproduce observed patterns.

Key observations include:

- A positive long-term trend in N_2O concentration is evident at most stations, consistent with ongoing increases in global N_2O emissions.
- All stations exhibit a consistent seasonal cycle, with N_2O mixing ratios peaking during the spring and summer months and declining during winter. This seasonality is likely driven by temperature-dependent biogenic emissions and atmospheric transport.
- After inversion, the posterior mixing ratios more closely follow the observed variability, where the red line aligns more tightly with the black observational data.
- The posterior simulations better capture episodic enhancements (e.g., local emission spikes), indicating improved representation of regional-scale emission hotspots that the prior failed to resolve.

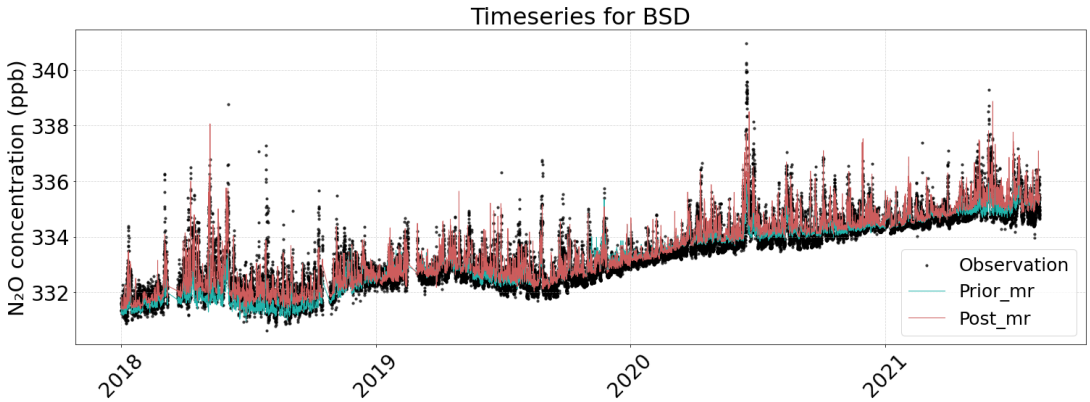

This project has received funding from the European Union's Horizon Europe research and innovation programme under grant agreement No 101081395

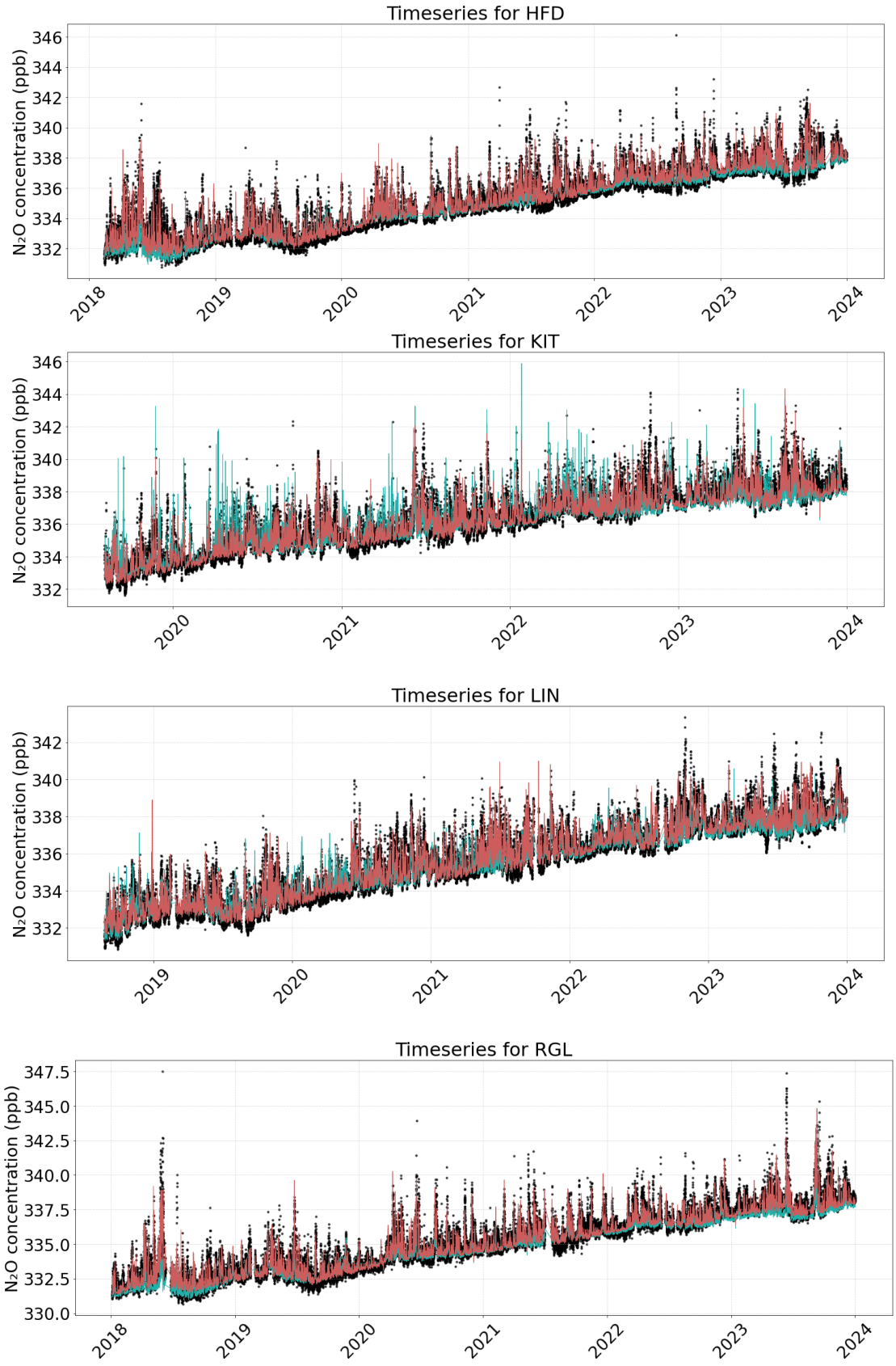

Figure 4.5: Time series of assimilated N_2O concentrations sampled at different stations used in the inversion. Assimilated measurement (black), CIF-FLEXPART Inversion results for posterior concentration (red), and prior concentration (green)

This project has received funding from the European Union's Horizon Europe research and innovation programme under grant agreement No 101081395

Figure 4.6 provides a comparative assessment of model performance before and after inversion across multiple monitoring stations, based on three key statistical metrics: Root Mean Square Error (RMSE), bias, and the coefficient of determination (R^2).

Top panel shows the Root Mean Square (RMSE) and bias:

- At most monitoring stations, the posterior simulations show a noticeable reduction in RMSE compared to the prior simulations, indicating an improvement in model accuracy after assimilation. For example, stations such as CBW, HUN, JUE, and LMP display clear reductions in error magnitude. However, some sites remain problematic—MHD stands out with the highest RMSE both before and after adjustment, though posterior assimilation still reduces the error somewhat.
- Bias (green bars) reflects systematic deviations. The prior simulations often show negative bias (light green), indicating that the model tends to underestimate observed concentrations. Posterior simulations (dark green) bring these values much closer to zero, effectively reducing systematic deviations. Stations such as CIB, HUN, KRE, and LMP exhibit particularly strong improvements in bias reduction, with posterior values aligning much better with observations.

Overall, posterior simulations consistently improve both error magnitude and systematic bias across the majority of stations. The magnitude of improvement, however, varies by location. While many stations benefit substantially, a few sites such as MHD and LMP remain challenging, suggesting that local conditions—such as unique meteorological dynamics, unaccounted emissions, or observational uncertainties—may be limiting performance. These stations warrant further targeted investigation to diagnose the causes of persistent discrepancies.

Bottom panel shows coefficient of determination (R^2):

- For most stations, posterior R^2 values (dark blue) are equal to or higher than the prior R^2 values, showing improvement in model performance after updating with data.
- A few stations (e.g., LUT, JUE, KIT, MHD) show more noticeable differences, where the posterior model significantly outperforms the prior.
- Many stations already had high prior R^2 values (>0.9), and the posterior adjustment only slightly improved them.
- Stations with lower prior R^2 (e.g., LUT, KIT, MHD) benefited most from the posterior correction.

The chart demonstrates that posterior simulations generally provide a better fit to observations across stations, meaning the data assimilation or Bayesian updating process successfully improved predictive performance. However, the improvement is station-dependent, with some locations showing more substantial gains than others.

This project has received funding from the European Union's Horizon Europe research and innovation programme under grant agreement No 101081395

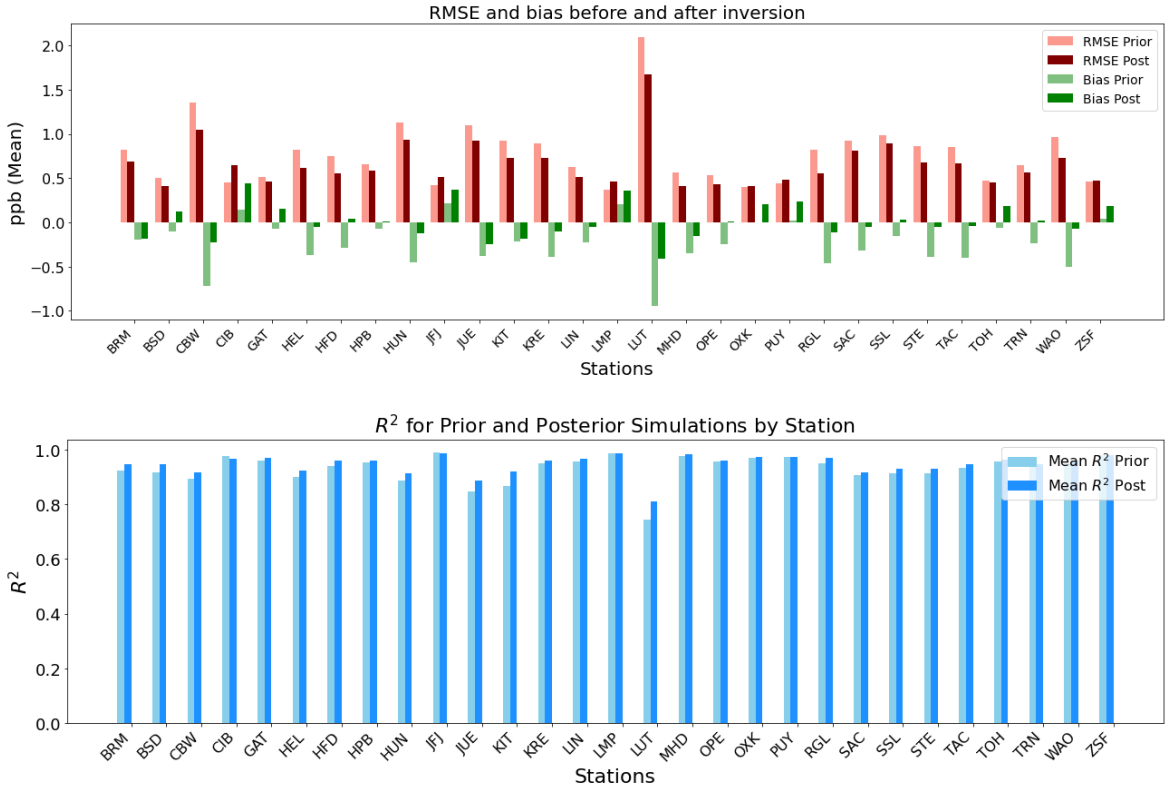

Figure 4.6: Statistical analysis of prior and posterior concentrations with observations for 2018-2023

4.4.2. Spatial distribution of prior and posterior emissions

Figure 4.7 compares prior and posterior estimates of mean N_2O emissions across Europe over the period 2018–2023. The left panel displays the prior emission estimates, while the right panel shows the posterior estimates after atmospheric inversion. The lower panel visualizes the difference between posterior and prior estimates, highlighting areas where corrections were made.

- Overall, emissions increase from 0.75 $TgN_2O\ yr^{-1}$ (prior) to 1.01 $TgN_2O\ yr^{-1}$ (posterior) for EU27+3, corresponding to an increase of ~34.7% after inversion.
- High-emission regions such as the Netherlands, western Germany, northwestern France, and the UK remain prominent in both prior and posterior estimates. This consistency underscores the strong and ongoing contribution from areas with intensive agriculture and livestock farming.
- Posterior estimates show substantially lower emissions over northern Italy, suggesting prior inventories overestimated N_2O sources in this region.
- The posterior-prior difference map indicates increased emissions in western France, Belgium, the Netherlands, and parts of Germany, while decreases are evident in Italy. These adjustments reflect constraints from observational data, particularly in agricultural hotspots.

This project has received funding from the European Union's Horizon Europe research and innovation programme under grant agreement No 101081395

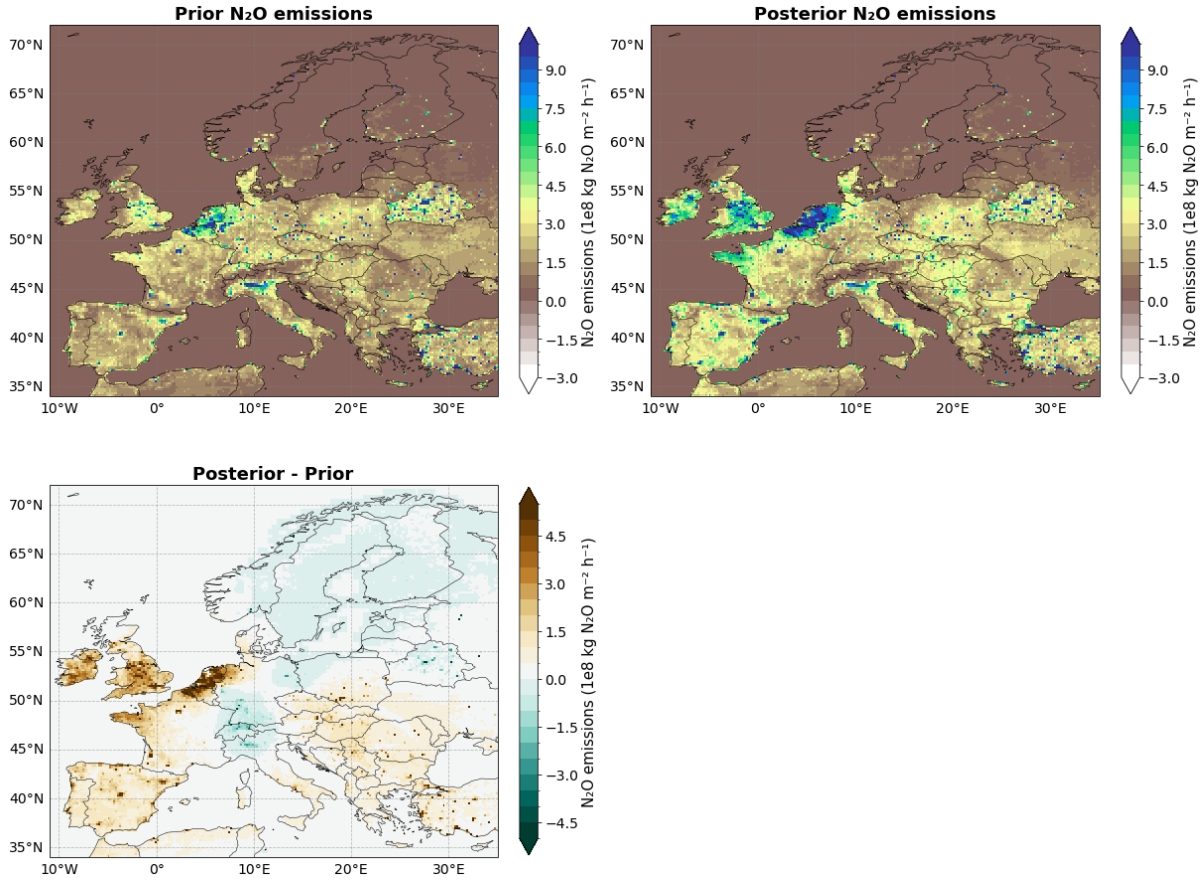

Figure 4.7: Mean spatial distribution of N_2O estimates from CIF-FLEXPART inversion at a higher resolution of 0.2°x 0.2° from 2018 to 2023: prior (left upper panel), posterior (right upper panel) and posterior increments computed as (posterior – prior) (lower panel).

Figure 4.8 shows the seasonal and interannual variability of total N_2O emissions for EU27+3 countries between 2018 and 2023, comparing the prior inventory with posterior inversion estimates at 0.2° and 0.5° spatial resolution. Both the prior (brown line) and posterior (green line) emissions exhibit a clear seasonal cycle, characterized by:

- peaks in late spring to early summer (May–June) linked to fertilizer application and warmer soil conditions enhancing microbial N_2O production.
- Troughs occur in winter, consistent with reduced microbial activity and lower fertilizer use.

Key observations include:

- Posterior estimates consistently exceed prior inventories across most years, revealing systematic underestimation in bottom-up inventories.
- The two posterior solutions (0.2° and 0.5°) are closely aligned in phase, exhibiting nearly identical seasonal timing. Differences are primarily in magnitude: the 0.2° inversion generally shows more pronounced and occasionally higher peaks, reflecting greater sensitivity to short-term variability, whereas the 0.5° inversion is smoother with slightly attenuated peak amplitudes, consistent with the effects of spatial aggregation.
- The year 2018 shows a decline in emissions from June to July and lower emissions for July to August compared to other years, likely due to widespread drought suppressing microbial production of N_2O and, possibly also reduced fertilizer usage.

This project has received funding from the European Union's Horizon Europe research and innovation programme under grant agreement No 101081395

The consistent seasonal cycle highlights the climatic control of N_2O emissions, while interannual variability reflects the influence of extreme weather, land management, and crop–fertilizer dynamics. Posterior estimates provide a more realistic representation of the European N_2O budget, emphasizing the importance of inverse modelling for correcting biases in bottom-up inventories.

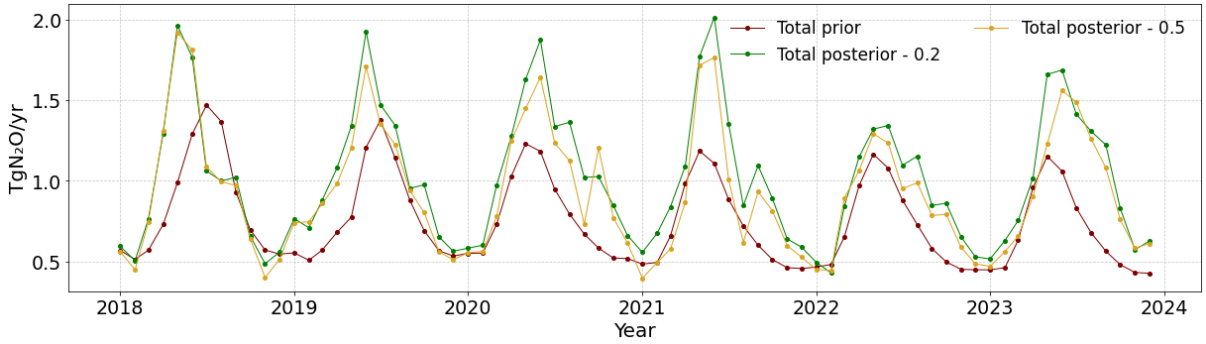

*Figure 4.8: Times series of monthly N_2O in Tg(N_2O)/year for the inversion period from 2018 to 2023 for **0.2°** and **0.5°** spatial resolution, for the EU-27+UK+Norway+Switerland area.*

5. CO_2 inversions

This section describes the final inversions of the CO_2 land ecosystem fluxes at a 0.2°×0.2° resolution. These final inversions cover the period 2019 to 2022. They rely on a configuration of the CIF-CHIMERE inversion system, following the new protocol for CO_2 regional inversions established in the frame of EYE-CLIMA (see the Appendix of D3.2).

The datasets used for these final inversions at the 0.2°×0.2° resolution, described in the protocol, better account for different types of fluxes, including fluxes to the atmosphere from fires, from inland waters and from harvested wood and crops. In particular, harvest fluxes provided by ORCHIDEE now have a more realistic spatial distribution (see Section 5.1.3). As boundary conditions have a strong impact on the annual NEE budgets (see D3.1), our inversions also now better account for them and for their uncertainties. The CO_2 inversion results have been derived with this new inversion configuration by assimilating surface observations (mainly from ICOS sites).

This section details the CIF-CHIMERE inversion configuration and the analysis of the system behaviour and of the resulting land ecosystem flux estimates. In line with the objective of these inversions, which should provide a benchmark for further developments and analysis in EYE-CLIMA, the presentation focuses on general patterns of the spatial variability of the corrections applied to the prior terrestrial ecosystem fluxes from surface, on the seasonal cycle and on the inter-annual variability of annual NEE budget for the European Union + UK + Switzerland + Norway (EU-27+3), i.e., on the type of general diagnostics analysed in recent inter-comparisons of European scale inversions (Monteil et al., 2020, Thompson et al., 2020, McGrath et al., 2023) and in D3.2.

5.1 Inverse modelling system and experimental framework

The inversion system relies on the coupling between the variational mode of the Community Inversion Framework (CIF, Berchet et al., 2021), the regional chemistry transport model CHIMERE (Menut et al., 2013; Mailler et al., 2017) and the adjoint of this model (Fortems-Cheiney et al., 2021b). The same

This project has received funding from the European Union's Horizon Europe research and innovation programme under grant agreement No 101081395

products as in D3.2 have been used for all the needed input data and described in the following sections. All the data have been here gridded to 0.2° × 0.2°.

5.1.1 Configuration of the regional CHIMERE chemistry-transport model for the simulation of CO_2 mole fractions over Europe

A European configuration of CHIMERE is used, covering latitudes 32.1-72.9°N and longitudes 14.9°W - 34.9°E with a 0.2°×0.2° horizontal resolution and 29 vertical layers up to 300 hPa. This domain is presented in Figure 1. This configuration corresponds to a number of grid-cells of 250 (longitude) x 205 (latitude) x 29 (altitude) = 1 486 250, about 10 times higher than the one for the 0.5° configuration in D3.1 and D3.3 (with about 137 360 grid-cells).

The inversions generally do not take the atmospheric source of CO_2 from the oxidation of CO into account, assuming this source is negligible. As the impact of this atmospheric CO source of CO_2 on the CO_2 concentrations and on the CO_2 land ecosystem fluxes estimated from the inversions is negligible (MS3), CO_2 is still considered as a passive tracer at the time scales considered in this study.

Consequently, when using the CHIMERE CTM and its adjoint code, here, only the atmospheric transport modelling components are used, and the chemistry modelling components are disactivated.

5.1.2 Land biosphere fluxes

Two products are used to derive prior or fixed estimates of the land-biosphere fluxes of CO_2:

ORCHIDEE simulation CRUERA-v5 at 0.125° resolution over Europe (35°-73°N and 25°W-45°E) and at hourly temporal resolution, providing:

- NPP and Rh at 3-hour resolution
- F_{LUC} (land use change fluxes restricted, here in practice, to emissions of carbon due to deforestation)
- local emissions of the total amount of carbon removed (without spatial displacement in ORCHIDEE) from the local carbon stocks by wood and crop harvest: $F_{WOODHARVEST}$ and $F_{CROPHARVEST}$ at annual resolution but spread at 1-hour resolution as a constant flux over the year

GFASv1.2 estimate of net biomass burning emissions at 0.1° resolution, until year 2025:

- F_{BB} at 1-day resolution

The F_{BB} fluxes from GFAS are used as a fixed flux component in the inversions.

5.1.3 Land fluxes from the "lateral" export of carbon from the ecosystems

The estimate of land fluxes due to "lateral" export of carbon from the ecosystems are derived using the last version of the database of Ciais et al. (2021). These estimates are provided globally at 0.083°x0.083° and 1-year resolution over 1961-2022. The estimates for 2022 have been used to impose the values for 2023. The following selection of fluxes from this database have been used:

- ALLWOODSOURCE (emissions from wood biofuel combustion and other wood products)
- ALLCROPSOURCE (emissions from crop biofuel combustion and other crop products such as human/animal respiration)
- ALLCROPSINK (estimate of the carbon sink corresponding to the crop harvest)
- ALLWOODSINK (estimate of the carbon sink corresponding to the wood harvest)
- RIVERSINK (transfer from soils to rivers)
- LAKERIVEREMIS (inland water outgassing)

This project has received funding from the European Union's Horizon Europe research and innovation programme under grant agreement No 101081395

5.1.4 Prior and fixed estimates of the land fluxes

For the sake of consistency between the sinks and sources associated to these lateral transfers in the prior estimate of the fluxes, the prior estimate of the NEE from ORCHIDEE is adjusted by adding a linear scaling of the ORCHIDEE $F_{CROPHARVEST}$ and $F_{WOODHARVEST}$ fields α x ($F_{CROPHARVEST}$ or $F_{WOODHARVEST}$) with α_{crop} and α_{wood} respectively defined so that the integral of this correction over Europe and the year equals the differences between the EU27+3 and 1-year scale budget of $F_{CROPHARVEST}$ and $F_{WOODHARVEST}$ versus the ALLCROPSINK and ALLWOODSINK estimates from Ciais et al. (2021), implicitly assuming that the budget from the latter is more accurate. Of note is that there is no sub-annual temporal resolution for the $F_{CROPHARVEST}$ and $F_{WOODHARVEST}$ fields out of the ORCHIDEE simulations. Therefore, these fluxes are prescribed as constant fluxes within a year, which thus applies to the adjustment of ORCHIDEE.

The estimates of $F_{WOODSOURCE}$ (=ALLWOODSOURCE), $F_{CROPSOURCE}$ (=ALLCROPSOURCE), and $F_{LAKERIVER}$ (=LAKERIVEREMIS+RIVERSINK) are used as a fixed flux components in the inversions. The ORCHIDEE $F_{CROPHARVEST}$ and $F_{WOODHARVEST}$ from ORCHIDEE themselves, which are redundant with the ALLWOODSOURCE and ALLCROPSOURCE but which are assumed to rely on a less accurate estimate of the harvests, and which ignore the import/export of harvest across the boundaries of Europe, are discarded.

5.1.5 Fossil emissions

Anthropogenic emissions from EDGARv8 are used as recommended by WP2 (MS 2). These are provided at monthly resolution for the following sectors (the sector codes are given in parentheses): i) Energy for buildings (BUILDINGS), ii) Fuel exploitation (FUEL_EXPLOITATION), iii) Industrial combustion (IND_COMBUSTION), iv) Industrial processes (IND_PROCESSES), v) Power industry (POWER_INDUSTRY), vi) Transport (TRANSPORT) and vii) Waste (WASTE).

EDGARv8 provides separate estimates for CO_2 emissions from fossil sources (F_{CO2}) versus bio-fuel sources for the above sectors. The biofuel files include “CO2bio” in the file name and are excluded. EDGARv8 provides weekly and hourly profiles per country and source sector, which should be used to calculate hourly varying emissions. The estimates for 2021 are used to impose the values for more recent years.

The F_{CO2} flux from EDGARv8 are used as a fixed flux component in the inversions.

5.1.6 Open and coastal ocean fluxes

The estimate of sea/ocean fluxes within the inversion domain is based on a hybrid product combining the coastal ocean flux estimates from the University of Bergen and a global ocean estimate from MPI-BGC-Jena (Rödenbeck et al., 2014; McGrath et al., 2023). The data is provided from 2005 to 2020 at a 0.125°×0.125° horizontal resolution and at daily temporal resolution. The estimates for 2020 are used to impose the values for more recent years.

This product is used as a prior estimate of the F_{OCEAN} fluxes in the inversions.

5.1.7 Prior / Fixed estimate of the boundary conditions and completion of the stratosphere

For the estimate of the prior initial, lateral and top boundary conditions, inversions use the CAMS global greenhouse gas inversion product, v22r1 available up to 2022-12.

5.1.8 Meteorological forcing

The CHIMERE CTM is driven by European Centre for Medium-Range Weather Forecasts (ECMWF) meteorological forecasts.

This project has received funding from the European Union's Horizon Europe research and innovation programme under grant agreement No 101081395

5.2. Observations

5.2.1. Near-surface in-situ measurements

As in D3.2, the inversion assimilates measurements of CO_2 mole fraction from the European Obspack compilation of atmospheric carbon dioxide data from ICOS and non-ICOS European ground based continuous measurement stations called “obspack_co2_466_GVeu_v10_20240729” (ICOS RI et al., 2024).

Following the protocol, usual observation selection strategies (Broquet et al., 2013, Monteil et al., 2020) the inversion assimilates 1-hour averages of the measured CO_2 mole fractions during the time windows 12:00-17:00 UTC for low altitude stations (below 1000 masl) and 0:00-6:00 UTC for high altitude stations (above 1000 masl). When several levels of measurements are available at a given station, the inversions assimilate the data from the highest level only.

The stations selected for the period 2019-2022 are shown in Figure 5.1. We have excluded the urban stations HEI (Heidelberg in Germany) and GIF (Gif sur Yvette in France) and some stations which are challenging to represent with meso-scale atmospheric transport models and/or which provide data over relatively short time over the entire period (LMU, VAC, GIC, SGC and EEC in Spain) from the dataset.

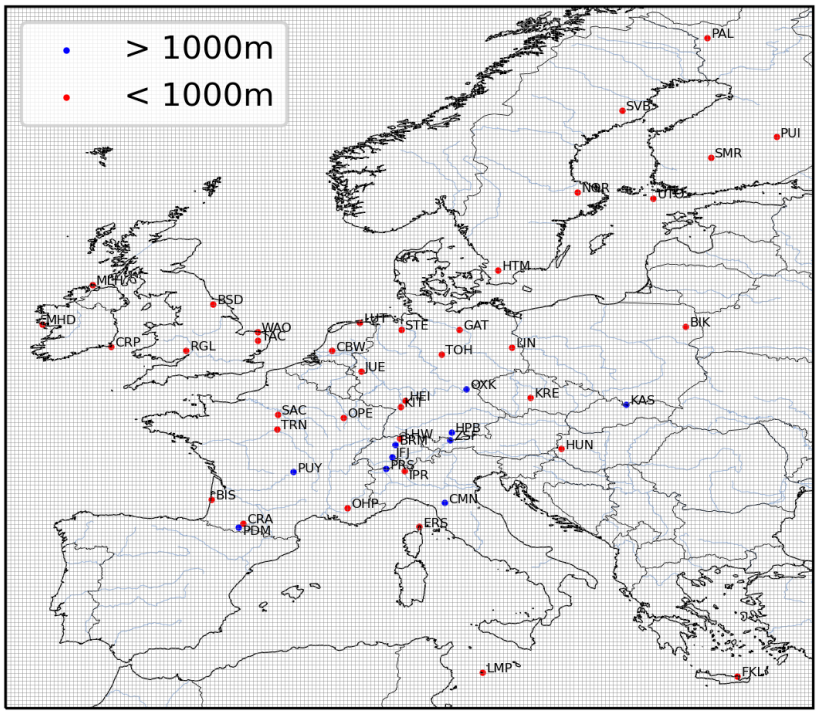

Figure 5.1: Domain and location of the observation sites. The colours indicate if the altitude (height above ground + sampling height) of the station is lower (in red) or higher (in blue) than 1000m.

5.3. The inversion framework

The inversions of CO_2 land ecosystem fluxes consist here in correcting the "prior" estimate of the sum of the Net Ecosystem Exchange (NEE) and of the fluxes F_{LUC} of CO_2 due to the Land Use Change (LUC), being limited here to emissions from deforestation. This prior estimate is corrected to derive “posterior” estimates with an improved fit between CHIMERE and the surface measurements of CO_2 mole fractions or XCO_2 satellite observations.

This project has received funding from the European Union’s Horizon Europe research and innovation programme under grant agreement No 101081395

Series of independent 1-month inversions have been performed to provide a posterior estimate of NEE+F_{LUC} from 2019 to 2022.

The inversion optimizes 6-hourly mean NEE+F_{LUC} fluxes at the 0.2°×0.2° resolution of CHIMERE. The uncertainty covariance matrix associated to the prior estimate of NEE+F_{LUC} is specified using the ORCHIDEE heterotrophic respiration, similarly to what is classically done in CO_2 inversions over Europe (Broquet et al., 2011; Monteil et al., 2020). Following the diagnostics of Kountouris et al. (2015), the temporal and spatial correlation scales for the uncertainty in the prior NEE+F_{LUC} (the prior uncertainty) are set to ≈1 month and 200 km, with no correlation between the four 6-hour windows of the same day. The inversions also control the ocean fluxes and the initial and lateral boundary conditions (see Table 4 of the protocol in the Appendix of D3.2).

The observation error covariance matrix characterizing the transport model and CO_2 measurement is set-up to be diagonal, ignoring the correlations between errors for different hourly averages of the CO_2 measurements (which has been justified by the analysis of Broquet et al., 2011. The variance of the observation errors corresponding to individual observations correspond to the Root Sum Square of the observation error values assigned to characterize the transport model error (see Table 3 of the protocol in the Appendix of D3.2).

The norm of the gradient of the cost function *J* is reduced by at least by 90% with the M1QN3 limited-memory quasi-Newton minimisation algorithm that we use (Gilbert and Lemaréchal, 1989).

5.4. Results

5.4.1. Fit to the assimilated observations

The reduction of the misfits between the simulation and the assimilated observations due to the corrections applied by the CIF-CHIMERE surface-based inversions to the prior estimates of the NEE+F_{LUC} and ocean fluxes and of the boundary conditions is illustrated in Table 5.1 for the month of July, from 2019 to 2022. When taking all the selected hourly observations of the stations into account in the year, the determinant coefficient R^2 is increased and the RMSE and the bias (from the prior to the posterior simulations) misfits between simulated versus measured CO_2 during the assimilation windows are always reduced (Table 5.1). Corrections to the NEE+F_{LUC} fluxes seem to conduct to a clear improvement of the fit of simulated mole fractions to the observations. These results raise a good confidence in the posterior NEE+F_{LUC} estimates, whose main characteristics are presented in the following sections.

Table 5.1: Statistics on the performance of the CHIMERE CTM compared to assimilated mole fraction measurements, before and after the inversions. Mean prior, posterior and relative difference (RDiff) of determinant coefficient (R^2), Root mean squared error (RMSE) and bias, considering all the selected hourly measurements, for the month of July, from 2019 to 2022.

	r			RMSE (ppm)			Bias (ppm)		
July	**Prior**	**Post**	**rdiff**	**prior**	**post**	**rdiff**	**prior**	**post**	**rdiff**
2019	0.20	0.42	+104%	9.15	4.71	-48%	3.40	1.74	-49%
2020	0.09	0.26	+181%	20.49	5.64	-72%	8.05	-0.45	-94%
2021	0.05	0.13	+140%	19.04	7.3	-62%	3.92	-3.06	-22%
2022	0.13	0.18	+44%	26.43	6.53	-75%	11.42	0.11	-99%

This project has received funding from the European Union's Horizon Europe research and innovation programme under grant agreement No 101081395

5.4.2. Spatial variability of the annual corrections to the prior terrestrial ecosystem fluxes

Figure 5.2 presents maps of the annual corrections provided by the inversions to the adjusted ORCHIDEE CRUERA prior estimates for NEE+F_{LUC} when assimilating surface measurements from 2019 to 2022. Contrarily to the inversions using surface measurements at the 0.5° resolution showing positive corrections (D3.2), the inversions here show strong negative corrections to the prior estimates over Southern France, northern Italy, Switzerland, Germany and over Central Europe (i.e., Poland, Czech Republic, Austria, Slovakia). However, these negative corrections are in better agreement with the inversions using satellite observations at the 0.5° resolution in D3.2.

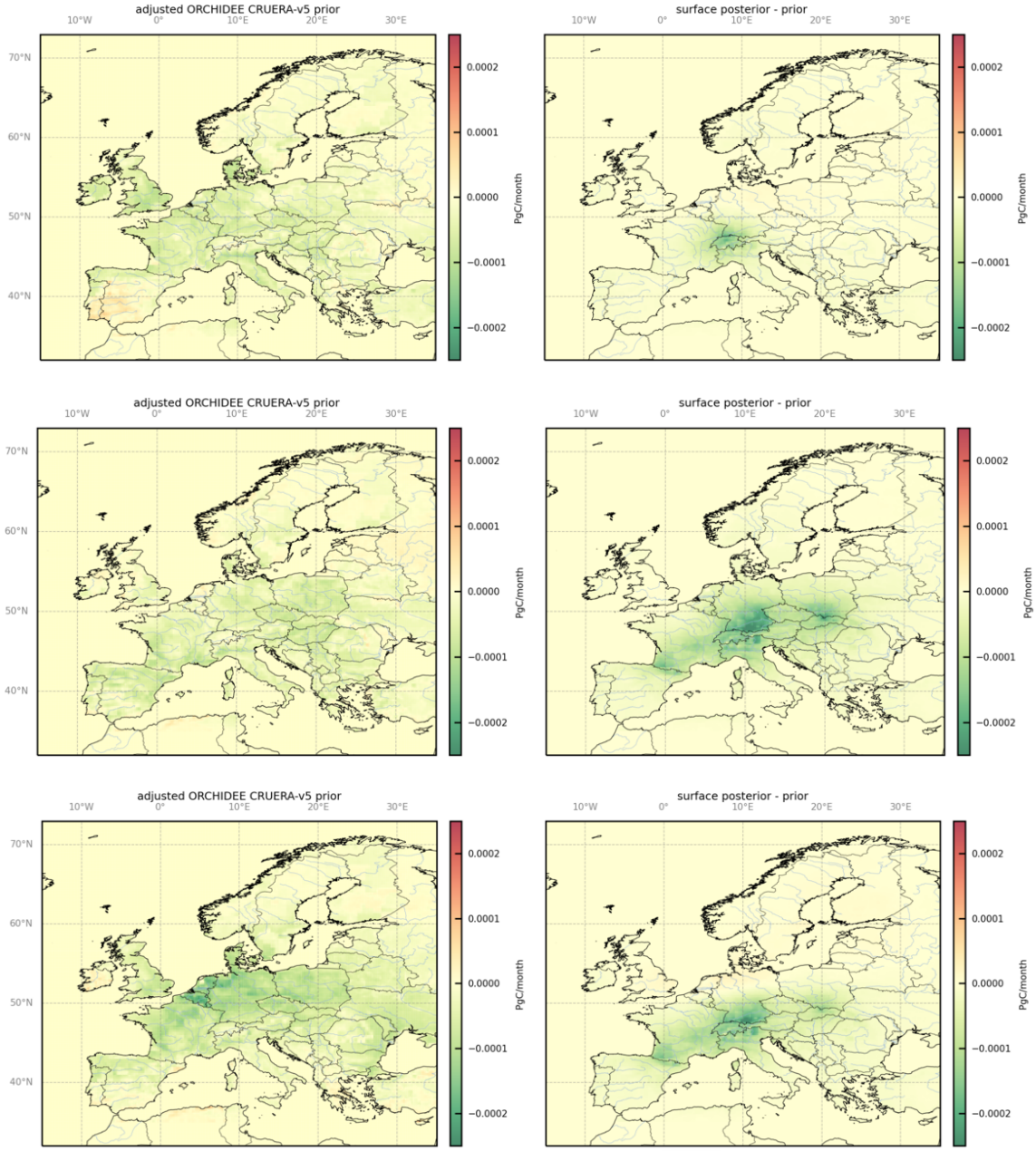

This project has received funding from the European Union's Horizon Europe research and innovation programme under grant agreement No 101081395

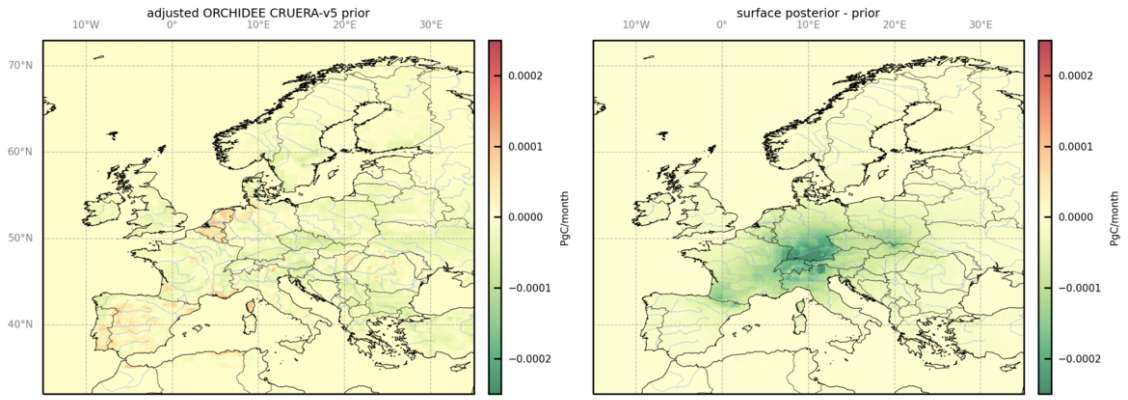

Figure 5.2: Maps of the adjusted ORCHIDEE CRUERA-v5 NEE+F_{LUC} prior estimates and of the annual corrections provided by the inversions to these priors when assimilating surface measurements, in PgC/year, from 2019 to 2022.

5.4.3. Seasonal cycle of the EU-27+3 NEE+F_{LUC} budget

Figure 5.3 presents a times series of monthly estimates of the CO_2 NEE+F_{LUC} from prior and posterior estimates from surface measurements, from January 2019 to December 2022.

The CO_2 positive maximum is always in October in the prior estimates. It can be in October (in 2021, 2022) or with a 1-month gap in November (in 2019, 2020) in the posterior estimates from the surface-based inversions. The maximum of the CO_2 peak uptake is often identified in May, both in the prior estimates and in the posterior estimates (except in 2019). Similarly to our NEE flux estimates from the inversion at 0.5° resolution, our NEE flux estimates are lower than the ones from ORCHIDEE at the end of summer.

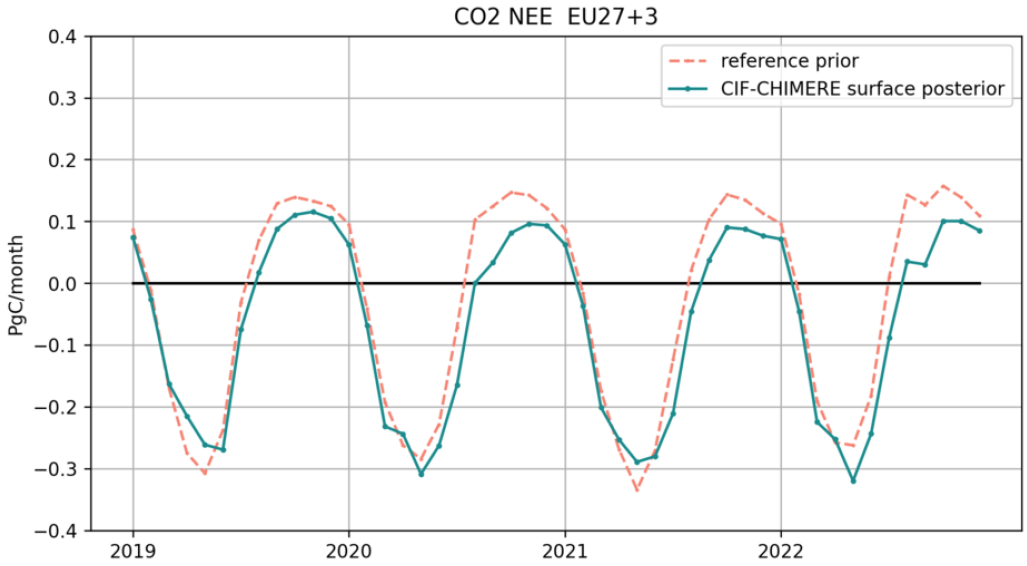

Figure 5.3: Times series of monthly estimates of the CO_2 NEE+FLUC, in PgC/month, from 2015 to 2023, for the EU-27+3 area. The dashed orange line is for the adjusted ORCHIDEE-CRUERA-v5 prior while the solid green line is for posterior estimates.

5.4.4. Inter-annual variability of the EU27+3 NEE+F_{LUC} budget

The posterior estimates of the NEE+F_{LUC} average annual budget for EU27+3 over the period 2019-2022 from the surface measurements at the 0.2° spatial resolution is about -0.78 PgC.yr^{-1}.

This project has received funding from the European Union's Horizon Europe research and innovation programme under grant agreement No 101081395

These estimates are 53% larger than the posterior estimates from surface measurements at the 0.5° spatial resolution of about -0.36 PgC.yr^{-1} over the period 2019-2022. However, as seen in Section 5.4.3, these estimates are relatively consistent with the posterior estimates from satellite observations at the 0.5° spatial resolution of about -0.90 PgC.yr^{-1} over the period 2019-2021.

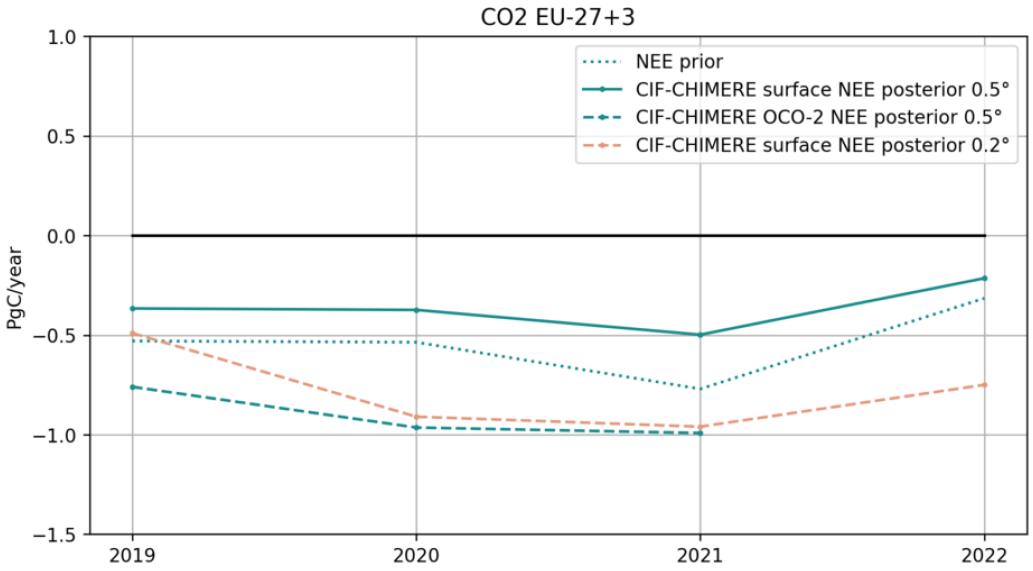

Figure 5.4: Times series of annual prior estimates of the CO_2 NEE+F_{LUC} and posterior estimates from the surface-based inversions at the 0.2° spatial resolution, in PgC/year, from January 2019 to December 2022 for the EU27+3 area. Posterior estimates from the surface- and satellite-based inversions at the 0.5° spatial resolution are also shown for comparison.

6. Deviations from the Description of Action

Because of the high computational cost of the CO_2 inversions at high resolution, these inversions have only been performed for the 2019-2022 period instead of 2018-2023 as initially planned. The extension of these inversions to 2018 and 2023 will be achieved in the coming weeks.

7.Conclusions

The CH_4 inversion within the CIF-FLEXPART framework for 2018–2023, performed at 0.2° × 0.2° resolution using a 4D-Var approach with FLEXPART-derived source–receptor relationships, optimized sector-specific methane fluxes by assimilating in situ observations. Posterior CH_4 mixing ratios show improved agreement with observations, with reduced bias and RMSE and higher correlations across all stations compared to the prior. The posterior fluxes suggest that prior inventories underestimated agricultural and combustion emissions in parts of northwestern and central Europe, while overestimating emissions in regions such as Italy, Romania, and the UK. Geological emissions are generally revised downward, emphasizing the need for region-specific scaling rather than uniform global factors. In contrast to the 0.5° inversion, geological emissions in this higher-resolution inversion are consistently corrected downward. Further investigation is needed to determine whether this discrepancy arises from the change in spatial resolution or from differences in the number of assimilated observation stations. Wetland emissions also decrease, particularly in northern Europe during summer, indicating prior overestimation of seasonal CH_4 release. Seasonal cycles remain consistent, with wetlands driving summer emission peaks. The total mean emission for the EU27+3 in the years 2018-2023 decrease

This project has received funding from the European Union's Horizon Europe research and innovation programme under grant agreement No 101081395

slightly from the prior estimate of 21.3 Tg yr^{-1} to a posterior estimate of 21.8 Tg yr^{-1}. However, substantial sectoral adjustments are evident: agricultural emissions increase by 17.1% (from 13.0 to 15.2 Tg yr^{-1}), geological emissions decline by 59.7% (from 2.6 to 1.0 Tg yr^{-1}), and wetland emissions decrease by 4.9% (from 3.7 to 3.6 Tg yr^{-1}).

N_2O inversion using the CIF–FLEXPART inversion framework at 0.2° resolution indicates systematically higher posterior emissions than the prior, with EU27+3 totals increasing from 0.75 TgN_2O yr^{-1} (prior) to 1.01 TgN_2O yr^{-1} (posterior), corresponding to an overall increase of ~34.67% after optimisation. The largest positive adjustments occur in northwestern Europe, notably across the UK, northern France and Benelux region, indicating that the prior likely underestimated emissions in these source areas. In contrast, the inversion suggests reduced emissions over parts of northern Italy and central–eastern Europe, pointing to potential prior overestimation or redistribution of sources in these regions. Model–data evaluation indicates a clear improvement from prior to posterior. The posterior simulations show stronger agreement with observed mixing ratios, with consistently high station-wise performance (R^2 close to 1 at most sites) and an overall reduction in RMSE alongside bias moving closer to zero at many stations. Together, these results support a successful inversion, yielding a spatially coherent posterior emission field and improved reproduction of observed variability, while also implying that the prior inventory underestimates total European N_2O emissions by roughly one-third for the analysed period.

CO_2 inversions using the CIF-CHIMERE model at the 0.2° spatial resolution to correct prior estimates of the Net Ecosystem Exchange (NEE) and of the ocean fluxes and of the boundary conditions by assimilating surface observations show that the model significantly improves the fit between simulated and observed CO_2 concentrations, reducing root-mean-square (RMS) errors and biases. The posterior estimates of the NEE+F_{LUC} average annual budget for EU27+3 over the period 2019-2022 from the surface measurements at the 0.2° spatial resolution is of about -0.78 $PgC.yr^{-1}$. Contrary to the surface-based inversions at the 0.5° spatial resolution described in D3.2, the surface-based inversions at the 0.2° spatial resolution indeed result in negative corrections, relatively consistently with the satellite-based inversions at the 0.5° spatial resolution. Further work seems therefore needed to fully understand the impact of the spatial resolution on the NEE+F_{LUC} posterior estimates.

This project has received funding from the European Union's Horizon Europe research and innovation programme under grant agreement No 101081395

8. References

Apadula, F., Arnold, S., Bergamaschi, P., Biermann, T., Blanc, P.-E., Brunner, D., Chen, H., Chmura, L., Colomb, A., Conil, S., Couret, C., Cristofanelli, P., De Mazière, M., Delmotte, M., Emmenegger, L., Forster, G., Frumau, A., Gerbig, C., Gheusi, F., … ICOS ERIC. (2022). *European atmospheric CO2 and CH4 Mole Fraction data product - 2022* (Version 1.0). ICOS ERIC -- Carbon Portal. https://doi.org/10.18160/1RE0-2GKH

Berchet, A., Sollum, E., Thompson, R. L., Pison, I., Thanwerdas, J., Broquet, G., Chevallier, F., Aalto, T., Berchet, A., Bergamaschi, P., Brunner, D., Engelen, R., Fortems-Cheiney, A., Gerbig, C., Groot Zwaaftink, C. D., Haussaire, J.-M., Henne, S., Houweling, S., Karstens, U., Kutsch, W. L., Luijkx, I. T., Monteil, G., Palmer, P. I., van Peet, J. C. A., Peters, W., Peylin, P., Potier, E., Rödenbeck, C., Saunois, M., Scholze, M., Tsuruta, A., and Zhao, Y.: The Community Inversion Framework v1.0: a unified system for atmospheric inversion studies, Geoscientific Model Development, 14, 5331–5354, https://doi.org/10.5194/gmd-14-5331-2021, 2021.

Bergamaschi, P., Karstens, U., Manning, A. J., Saunois, M., Tsuruta, A., Berchet, A., Vermeulen, A. T., Arnold, T., Janssens-Maenhout, G., Hammer, S., Levin, I., Schmidt, M., Ramonet, M., Lopez, M., Lavric, J., Aalto, T., Chen, H., Feist, D. G., Gerbig, C., Haszpra, L., Hermansen, O., Manca, G., Moncrieff, J., Meinhardt, F., Necki, J., Galkowski, M., O'Doherty, S., Paramonova, N., Scheeren, H. A., Steinbacher, M., and Dlugokencky, E.: Inverse modelling of European CH4 emissions during 2006–2012 using different inverse models and reassessed atmospheric observations, Atmospheric Chemistry and Physics, 18(2), 901-920, https://doi.org/10.5194/acp-18-901-2018, 2018.

Broquet, G., F. Chevallier, P. Rayner, C. Aulagnier, I. Pison, M. Ramonet, M. Schmidt, A. T. Vermeulen, and P. Ciais, A European summertime CO_2 biogenic flux inversion at mesoscale from continuous in situ mixing ratio measurements, *J. Geophys. Res.*, 116, D23303, doi:10.1029/2011JD016202, 2011.

Ciais, P., Yitong Yao, Thomas Gasser, Alessandro Baccini, Yilong Wang, Ronny Lauerwald, Shushi Peng, Ana Bastos, Wei Li, Peter A Raymond, Josep G Canadell, Glen P Peters, Rob J Andres, Jinfeng Chang, Chao Yue, A Johannes Dolman, Vanessa Haverd, Jens Hartmann, Goulven Laruelle, Alexandra G Konings, Anthony W King, Yi Liu, Sebastiaan Luyssaert, Fabienne Maignan, Prabir K Patra, Anna Peregon, Pierre Regnier, Julia Pongratz, Benjamin Poulter, Anatoly Shvidenko, Riccardo Valentini, Rong Wang, Grégoire Broquet, Yi Yin, Jakob Zscheischler, Bertrand Guenet, Daniel S Goll, Ashley-P Ballantyne, Hui Yang, Chunjing Qiu, Dan Zhu, Empirical estimates of regional carbon budgets imply reduced global soil heterotrophic respiration, *National Science Review*, Volume 8, Issue 2, https://doi.org/10.1093/nsr/nwaa145, 2021.

Etiope, G., Ciotoli, G., Schwietzke, S., & Schoell, M.: Gridded maps of geological methane emissions and their isotopic signature, Earth System Science Data, 11(1), 1-22, https://doi.org/10.5194/essd-11-1-2019, 2019.

Errico, R. M.: What is an adjoint model?, Bulletin of the American Meteorological Society, 78(11), 2577-2591, 1997.

Fortems-Cheiney, A., Pison, I., Broquet, G., Dufour, G., Berchet, A., Potier, E., Coman, A., Siour, G., and Costantino, L.: Variational regional inverse modeling of reactive species emissions with PYVAR-CHIMERE-v2019, Geosci. Model Dev., 14, 2939–2957, https://doi.org/10.5194/gmd-14-2939-2021, 2021.

Gilbert, J. and Lemaréchal, C.: Some numerical experiments with variable storage quasi-Newton algorithms, Math. Program., 45, 407–435, https://doi.org/10.1007/BF01589113, 1989.

This project has received funding from the European Union's Horizon Europe research and innovation programme under grant agreement No 101081395

Hittmeir, S., Philipp, A., Seibert, P., & Makovec, F.: Preprocessing of meteorological data for Lagrangian modeling, Geoscientific Model Development, 11(7), 2739-2749, https://doi.org/10.5194/gmd-11-2739-2018, 2018.

ICOS RI, Bergamaschi, P., Colomb, A., De Mazière, M., Emmenegger, L., Kubistin, D., Lehner, I., Lehtinen, K., Leuenberger, M., Lund Myhre, C., Marek, M.V., O'Doherty, S., Platt, S.M., Plaß-Dülmer, C., Apadula, F., Arnold, S., Blanc, P.-E., Brunner, D., Chen, H., Chmura, L., Chmura, Ł., Conil, S., Couret, C., Cristofanelli, P., Forster, G., Frumau, A., Gerbig, C., Gheusi, F., Hammer, S., Haszpra, L., Hatakka, J., Heliasz, M., Henne, S., Hensen, A., Hoheisel, A., Kneuer, T., Larmanou, E., Laurila, T., Leskinen, A., Levin, I., Lindauer, M., Lopez, M., Mammarella, I., Manca, G., Manning, A., Martin, D., Meinhardt, F., Mölder, M., Müller-Williams, J., Noe, S.M., Nęcki, J., Ottosson-Löfvenius, M., Philippon, C., Pitt, J., Ramonet, M., Rivas-Soriano, P., Scheeren, B., Schumacher, M., Sha, M.K., Spain, G., Steinbacher, M., Sørensen, L.L., Vermeulen, A., Vítková, G., Xueref-Remy, I., di Sarra, A., Conen, F., Kazan, V., Roulet, Y.-A., Biermann, T., Delmotte, M., Heltai, D., Hermansen, O., Komínková, K., Laurent, O., Levula, J., Lunder, C., Marklund, P., Morguí, J.-A., Pichon, J.-M., Schmidt, M., Sferlazzo, D., Smith, P., Stanley, K., Trisolino, P., Zazzeri, G., ICOS Carbon Portal, ICOS Atmosphere Thematic Centre, ICOS Flask And Calibration Laboratory, ICOS Central Radiocarbon Laboratory, 2024. European Obspack compilation of atmospheric methane data from ICOS and non-ICOS European stations for the period 1984-2024; obspack_ch4_466_GVeu_v10.0_20240702. https://doi.org/10.18160/PAWA-B2Y4

ICOS RI, Bergamaschi, P., Colomb, A., De Mazière, M., Emmenegger, L., Kubistin, D., Lehner, I., Lehtinen, K., Leuenberger, M., Lund Myhre, C., Marek, M.V., O'Doherty, S., Platt, S.M., Plaß-Dülmer, C., Ramonet, M., Rennick, C., Schmidt, M., Zähle, S., Apadula, F., Arnold, S., Blanc, P.-E., Brunner, D., Chen, H., Chmura, Ł., Chmura, L., Conil, S., Cristofanelli, P., Di Iorio enea, T., Forster, G., Frumau, A., Gerbig, C., Gheusi, F., Hammer, S., Haszpra, L., Hatakka, J., Heliasz, M., Hensen, A., Hoheisel, A., Kneuer, T., Larmanou, E., Laurila, T., Leskinen, A., Levin, I., Levula, J., Lindauer, M., Lopez, M., Lunder, C., Mammarella, I., Manca, G., Manning, A., Martin, D., Meinhardt, F., Molnár, M., Mölder, M., Müller-Williams, J., Noe, S.M., Nęcki, J., Ottosson-Löfvenius, M., Philippon, C., Piacentino, S., Pitt, J., Rivas-Soriano, P., Scheeren, B., Schumacher, M., Sha, M.K., Smith, P., Spain, G., Steinbacher, M., Sørensen, L.L., Vermeulen, A., Vítková, G., Xueref-Remy, I., Zaehle, S., di Sarra, A., Conen, F., Henne, S., Kazan, V., Roulet, Y.-A., Biermann, T., Delmotte, M., Heltai, D., Hermansen, O., Komínková, K., Laurent, O., Marklund, P., Morguí, J.-A., Pichon, J.-M., Sferlazzo, D., Stanley, K., Trisolino, P., Zazzeri, G., ICOS Carbon Portal, ICOS Atmosphere Thematic Centre, ICOS Flask And Calibration Laboratory, ICOS Flask And Calibration Laboratory, ICOS Central Radiocarbon Laboratory, 2024. European Obspack compilation of atmospheric carbon dioxide data from ICOS and non-ICOS European stations for the period 1972-2024; obspack_co2_466_GVeu_v10.0_20240729. https://doi.org/10.18160/X450-GTAY

Kountouris, P., Gerbig, C., Totsche, K.-U., Dolman, A. J., Meesters, A. G. C. A., Broquet, G., Maignan, F., Gioli, B., Montagnani, L., and Helfter, C.: An objective prior error quantification for regional atmospheric inverse applications, Biogeosciences, 12, 7403–7421, https://doi.org/10.5194/bg-12-7403-2015, 2015.

Lanczos, C.: An iteration method for the solution of the eigenvalue problem of linear differential and integral operators, Journal of Research of the National Bureau of Standards, 45(4), 255-282, https://doi.org/10.6028/jres.045.026, 1950.

Mailler, S., Menut, L., Khvorostyanov, D., Valari, M., Couvidat, F., Siour, G., Turquety, S., Briant, R., Tuccella, P., Bessagnet, B., Colette, A., Létinois, L., Markakis, K., and Meleux, F.: CHIMERE-2017: from urban to hemispheric chemistry-transport modeling, Geosci. Model Dev., 10, 2397–2423, https://doi.org/10.5194/gmd-10-2397-2017, 2017.

McGrath, M. J., Petrescu, A. M. R., Peylin, P., Andrew, R. M., Matthews, B., Dentener, F., Balkovič, J., Bastrikov, V., Becker, M., Broquet, G., Ciais, P., Fortems-Cheiney, A., Ganzenmüller, R., Grassi, G., Harris, I., Jones, M., Knauer, J., Kuhnert, M., Monteil, G., Munassar, S., Palmer, P. I., Peters, G. P., Qiu,

This project has received funding from the European Union's Horizon Europe research and innovation programme under grant agreement No 101081395

C., Schelhaas, M.-J., Tarasova, O., Vizzarri, M., Winkler, K., Balsamo, G., Berchet, A., Briggs, P., Brockmann, P., Chevallier, F., Conchedda, G., Crippa, M., Dellaert, S. N. C., Denier van der Gon, H. A. C., Filipek, S., Friedlingstein, P., Fuchs, R., Gauss, M., Gerbig, C., Guizzardi, D., Günther, D., Houghton, R. A., Janssens-Maenhout, G., Lauerwald, R., Lerink, B., Luijkx, I. T., Moulas, G., Muntean, M., Nabuurs, G.-J., Paquirissamy, A., Perugini, L., Peters, W., Pilli, R., Pongratz, J., Regnier, P., Scholze, M., Serengil, Y., Smith, P., Solazzo, E., Thompson, R. L., Tubiello, F. N., Vesala, T., and Walther, S.: The consolidated European synthesis of CO2 emissions and removals for the European Union and United Kingdom: 1990–2020, Earth Syst. Sci. Data, 15, 4295–4370, https://doi.org/10.5194/essd-15-4295-2023, 2023.

Meirink, J. F., Bergamaschi, P., and Krol, M. C.: Four-dimensional variational data assimilation for inverse modelling of atmospheric methane emissions: method and comparison with synthesis inversion, Atmospheric Chemistry and Physics, 8(21), 6341–6353, https://doi.org/10.5194/acp-8-6341-2008, 2008.

Menut, L., Bessagnet, B., Khvorostyanov, D., Beekmann, M., Blond, N., Colette, A., Coll, I., Curci, G., Foret, G., Hodzic, A., Mailler, S., Meleux, F., Monge, J.-L., Pison, I., Siour, G., Turquety, S., Valari, M., Vautard, R., and Vivanco, M. G.: CHIMERE 2013: a model for regional atmospheric composition modelling, Geosci. Model Dev., 6, 981–1028, https://doi.org/10.5194/gmd-6-981-2013, 2013.

Monteil, G., Broquet, G., Scholze, M., Lang, M., Karstens, U., Gerbig, C., Koch, F.-T., Smith, N. E., Thompson, R. L., Luijkx, I. T., White, E., Meesters, A., Ciais, P., Ganesan, A. L., Manning, A., Mischurow, M., Peters, W., Peylin, P., Tarniewicz, J., Rigby, M., Rödenbeck, C., Vermeulen, A., and Walton, E. M.: The regional European atmospheric transport inversion comparison, EUROCOM: first results on European-wide terrestrial carbon fluxes for the period 2006–2015, Atmos. Chem. Phys., 20, 12063–12091, https://doi.org/10.5194/acp-20-12063-2020, 2020.

Petrescu, A. M. R., McGrath, M. J., Andrew, R. M., Peylin, P., Peters, G. P., Ciais, P., Broquet, G., Tubiello, F. N., Gerbig, C., Pongratz, J., Janssens-Maenhout, G., Grassi, G., Nabuurs, G.-J., and Dolman, A. J.: The consolidated European synthesis of CH4 and N2O emissions for the European Union and United Kingdom: 1990–2017, Earth System Science Data, 13(5), 2307–2362, https://doi.org/10.5194/essd-13-2307-2021, 2021.

Pisso, I., Sollum, E., Grythe, H., Kristiansen, N. I., Cassiani, M., Eckhardt, S., Arnold, D., Morton, D., Thompson, R. L., Zwaaftink, C. D. G., Evangeliou, N., Sodemann, H., Haimberger, L., Henne, S., Brunner, D., Burkhart, J. F., Fouilloux, A., Brioude, J., Philipp, A., Seibert, P., & Stohl, A.: The Lagrangian particle dispersion model FLEXPART version 10.4, Geoscientific Model Development, 12(12), 4955-4997, https://doi.org/10.5194/gmd-12-4955-2019, 2019.

Randerson, J. T., van der Werf, G. R., Giglio, L., Collatz, G. J., & Kasibhatla, P. S.: Global Fire Emissions Database, Version 4.1 (GFEDv4), ORNL DAAC, https://doi.org/10.3334/ORNLDAAC/1293, 2017.

Rödenbeck, C., Bakker, D. C. E., Metzl, N., Olsen, A., Sabine, C., Cassar, N., Reum, F., Keeling, R. F., and Heimann, M.: Interannual sea–air CO_2 flux variability from an observation-driven ocean mixed-layer scheme, Biogeosciences, 11, 4599–4613, https://doi.org/10.5194/bg-11-4599-2014, 2014.

Saunois, M., Martinez, A., Poulter, B., Zhang, Z., Raymond, P., Regnier, P., Canadell, J.G., Jackson, R.B., Patra, P.K., Bousquet, P., Ciais, P., Dlugokencky, E.J., Lan, X., Allen, G.H., Bastviken, D., Beerling, D.J., Belikov, D.A., Blake, D.R., Castaldi, S., Crippa, M., Deemer, B.R., Dennison, F., Etiope, G., Gedney, N., Höglund-Isaksson, L., Holgerson, M.A., Hopcroft, P.O., Hugelius, G., Ito, A., Jain, A.K., Janardanan, R., Johnson, M.S., Kleinen, T., Krummel, P., Lauerwald, R., Li, T., Liu, X., McDonald, K.C., Melton, J.R., Mühle, J., Müller, J., Murguia-Flores, F., Niwa, Y., Noce, S., Pan, S., Parker, R.J., Peng, C., Ramonet, M., Riley, W.J., Rocher-Ros, G., Rosentreter, J.A., Sasakawa, M., Segers, A., Smith, S.J., Stanley, E.H.,

Schuldt KN, Aalto T, Arlyn Andrews A, Shuji JA, Baier B, Bergamaschi P, Biermann T, Biraud SC, Boenisch H, Brailsford G, Huilin Chen C. Multi-laboratory compilation of atmospheric methane data for

This project has received funding from the European Union's Horizon Europe research and innovation programme under grant agreement No 101081395

the period 1981-2024; obspack_ch4_1_GLOBALVIEWplus_v7.0_2024-10-29; NOAA Earth System Research Laboratory, Global Monitoring Laboratory. http://doi.org/10.25925/20241001.

Thanwerdas, J., Tian, H., Tsuruta, A., Tubiello, F.N., Weber, T.S., van der Werf, G., Worthy, D.E., Xi, Y., Yoshida, Y., Zhang, W., Zheng, B., Zhu, Qing, Zhu, Qiuan, Zhuang, Q., Global Methane Budget 2000-2020. Earth System Science Data Discussions 1–147. https://doi.org/10.5194/essd-2024-115, 2024.

Thompson, R.L., G. Broquet, C. Gerbig, T. Koch, M. Lang, G. Monteil, S. Munassar, A. Nickless, M. Scholze, M. Ramonet, U. Karstens, E. van Schaik, Z. Wu, C. Rödenbeck; Changes in net ecosystem exchange over Europe during the 2018 drought based on atmospheric observations. *Philos Trans R Soc Lond B Biol Sci* 26 October 2020; 375 (1810): 20190512. https://doi.org/10.1098/rstb.2019.0512, 2020.

Thompson, R. L., Groot Zwaaftink, C. D., Brunner, D., Tsuruta, A., Aalto, T., Raivonen, M., Crippa, M., Solazzo, E., Guizzardi, D., Regnier, P., and Maisonnier, M.: Effects of extreme meteorological conditions in 2018 on European methane emissions estimated using atmospheric inversions, Philosophical Transactions of the Royal Society A: Mathematical, Physical and Engineering Sciences, 380, 20200443, https://doi.org/10.1098/rsta.2020.0443, 2021.

Stohl, A., Wotawa, G., Seibert, P., & Kromp-Kolb, H.: Interpolation errors in wind fields as a function of spatial and temporal resolution and their impact on different types of kinematic trajectories, Journal of Applied Meteorology, 34(10), 2149-2165, https://doi.org/10.1175/1520-0450(1995)034<2149>2.0.CO;2, 1995.

Thompson, R. L., & Stohl, A.: COCCON: an international network to detect changes in carbon monoxide, Atmospheric Chemistry and Physics, 14(5), 2319-2342, https://doi.org/10.5194/acp-14-2319-2014, 2014.

Tipka, A., Hittmeir, S., Philipp, A., & Seibert, P.: Flex_extract v7.1.2 - a software package to retrieve and prepare ECMWF data for use in FLEXPART, Geoscientific Model Development, 13(11), 5277-5310, https://doi.org/10.5194/gmd-13-5277-2020, 2020.

Weber, T.: Estimates of global ocean methane emissions based on a spatially explicit global ocean methane model, Biogeosciences, 16(17), 3227-3244, https://doi.org/10.5194/bg-16-3227-2019, 2019.

This project has received funding from the European Union's Horizon Europe research and innovation programme under grant agreement No 101081395

https://eyeclima.eu

BRUSSELS, 17 02 2026

Funded by the European Union. Views and opinions expressed are however those of the author(s) only and do not necessarily reflect those of the European Union. Neither the European Union nor the granting authority can be held responsible for them.

This project has received funding from the European Union's Horizon Europe research and innovation programme under grant agreement No 101081395